

A STUDY OF UO_2 GRAIN BOUNDARY STRUCTURE AND THERMAL
RESISTANCE CHANGE UNDER IRRADIATION USING MOLECULAR
DYNAMICS SIMULATIONS

A Thesis

by

TIANYI CHEN

Submitted to the Office of Graduate Studies of
Texas A&M University
in partial fulfillment of the requirements for the degree of

MASTER OF SCIENCE

Chair of Committee,	Lin Shao
Committee Members,	Sean McDeavitt
	Xinghang Zhang
Head of Department,	Yassin Hassan

August 2013

Major Subject: Nuclear Engineering

Copyright 2013 Tianyi Chen

ABSTRACT

Our study is focused on the behavior of grain boundaries in uranium dioxide system under irradiation conditions. The research can be seen as two parts: the study of interaction of the grain boundary and the damage cascade, and the calculation of Kapitza resistance of grain boundaries. The connection between these two parts lies in that damage cascades bring in changes in the structure and other properties of grain boundaries, and inevitably the Kapitza resistance of the grain boundary changes as well. For the first part, we studied interactions of grain boundaries and damage cascades in uranium dioxide system by simulating two types of bombardments: one direct bombardment into a grain boundary leading to ballistic-collision-mediated interface mixing; the other bombardment is in the close vicinity of a grain boundary causing interface biased defect migration. We found that more defects are trapped by the grain boundary followed by the first type of bombardment, resulting in enhanced grain boundary energy. By comparing with the second type of bombardment, we are able to reveal the mechanisms of the interaction between defects and grain boundaries. For the second part, we employed the non-equilibrium molecular dynamics method to calculate the Kapitza resistance of different coincident site lattice boundaries with or without defects loaded, and later we found that a universal positive correlation between the Kapitza resistance and the grain boundary energy can be well established, regardless of the cause of boundary energy changes. Our study provides a deeper understanding of the Kapitza resistance of the grain boundary and its evolutions under irradiation, which

benefits multi-scale modeling of uranium dioxide thermal properties under extreme radiation conditions as well as experimental studies of fuel material thermal properties.

ACKNOWLEDGEMENTS

I would like to give my gratitude and respect to my advisor and committee chair, Dr. Shao, who offered me the most valuable guidance and help in my research. I would like to thank my committee members, Dr. McDeavitt and Dr. Zhang for their helps in my degree pursuing.

Thanks also go to my friends and colleagues and the department faculties and staffs for making my time at Texas A&M University a great experience. Especially to L. Price, D. Chen, C.C. Wei, J. Wang, Dr. Aitkaliveya and R. Jenson for their suggestions and helps throughout this thesis.

Finally, thanks go to my mother and father for their encouragement and support.

NOMENCLATURE

UO ₂	Uranium dioxide
GB	Grain boundary
MD	Molecular dynamics
SEM	Scanning electron microscopy
EBSD	Electron backscatter diffraction
CSL	Coincident site lattice
LAMMPS	Large-scale atomic/molecular massively parallel simulator
PKA	Primary knock-on atom
NEMD	Non-equilibrium molecular dynamics method
ZBL	Ziegler-Biersack-Littmark

TABLE OF CONTENTS

	Page
ABSTRACT	ii
ACKNOWLEDGEMENTS	iv
NOMENCLATURE	v
TABLE OF CONTENTS	vi
LIST OF FIGURES	viii
LIST OF TABLES	xii
 1. INTRODUCTION TO FUEL MATERIALS	 1
1.1 Oxide fuels	1
1.2 Ceramic fuels	6
1.3 Metallic fuels	9
1.4 Liquid fuels	13
 2. PREVIOUS RESEARCH IN UO_2 SYSTEM	 14
2.1 Experimental studies on thermal properties of UO_2	14
2.2 Simulation studies on thermal properties of monocrystal UO_2	21
2.3 Simulation studies focused on the presence of GBs	25
2.4 The motivation of our research	28
 3. MOLECULAR DYNAMICS SIMULATION	 29
3.1 An introduction to MD simulations	29
3.2 MD simulations of ion-solid interactions	31
3.3 MD simulations for thermal conductivities	36
3.4 Overview of classical interatomic potentials of UO_2 systems	40
 4. DAMAGE CASCADES IN BICRYSTAL UO_2 SYSTEM	 45
4.1 The Ziegler-Biesack-Littmark potential	46

4.2 The direct interaction of damage cascades and GBs	48
4.3 The indirect interaction of damage cascades and GBs.....	53
4.4 Conclusions and comparisons of direct and indirect interactions	56
5. THE KAPITZA RESISTANCE OF GRAIN BOUNDARIES	60
5.1 Simulation configurations and calculations of the Kapitza resistance	60
5.2 The Kapitza resistance and grain boundary energy of CSL boundaries	66
5.3 The effect of radiation damage on grain boundary properties	68
5.4 A correlation between the grain boundary Kapitza resistance and its energy	71
6. SUMMARY	74
REFERENCES.....	77

LIST OF FIGURES

	Page
Figure 1.1 PWR cross section views of (a) Surry fuel at 35 GW•d/t U and (b) Robinson fuel at 67 GW•d/t U	2
Figure 1.2 The center of a pellet of Robinson fuel at 67 GW•d/t U	3
Figure 1.3 A typical in-reactor volume change of fuel pellets	5
Figure 1.4 The porous structure formed in high burnup UO ₂ fuel	6
Figure 1.5 Volume increasing rates of uranium carbide fuels caused by solid fission products	7
Figure 1.6 A comparison of theoretical predicted and experimental measurement of the uranium carbide swelling	8
Figure 1.7 The increase of the length of various metallic fuels as a function of burnup level	10
Figure 1.8 The progressive improvement in the deformation of the cladding of metallic fuel elements	12
Figure 1.9 A diffusion couple of uranium and iron showing formation of intermetallic phases	12
Figure 2.1 The thermal conductivity of UO ₂ as a function on temperature	15
Figure 2.2 The phonon thermal conductivity of UO ₂ obtained from experiment compared to that computed using modified Leibfried-Schlomann equation	16
Figure 2.3 The thermal conductivity of UO ₂ as a function of O/U ratio at different temperatures	17
Figure 2.4 Experimental characterizations of GBs in a UO ₂ sample: (a) The SEM and EBSD image of the sample; (b) the length distribution of GB on misorientation angle; and (c) the length distribution on CSL boundaries	19
Figure 2.5 A schematic diagram for the interface thermal resistance (known as the Kapitza resistance) and the Kapitza length.....	20

Figure 2.6 Thermal properties calculated from MD simulations compared with experimental data	22
Figure 2.7 The “Bredig” transition in MD simulations: (a) a track of atoms with increasing temperatures; (b) mean square displacements of uranium and oxygen atoms as a function of temperature	23
Figure 2.8 Comparison of experimental and simulation data of thermal conductivity at different temperatures of the non-stoichiometric UO_{2+x} as a function of x...24	
Figure. 2.9 Thermal conductivity recovery (left) and Frenkel pairs recovery (right) during annealing for UO_2 system.....	25
Figure 2.10 Simulation study of thermal conductivities of polycrystalline UO_2 : (a) the structure of polycrystalline UO_2 system; (b) the Kapitza length of 3.8 nm grain polycrystalline UO_2 calculated from different potentials; (c) grain size dependent thermal conductivity from Yamada potential	26
Figure 2.11 Spatial distribution of point defects in different CSL GBs after relaxation of displacement cascades	27
Figure 3.1 A sketch of the algorithm of MD simulations	30
Figure 3.2 A sketch of ion-solid interaction.....	32
Figure 3.3 The nuclear stopping power and electronic stopping power as a function of ion velocity. V_0 is the Bohr velocity and Z_1 is the atomic number of the ion	33
Figure 3.4 Snapshots of a damage cascade in a ZrC matrix initialed by a PKA with initial energy of 50 keV	35
Figure 3.5 Calculations of thermal conductivities in UO_2 system by the Müller-Plathe method for different temperatures and different system sizes	39
Figure 3.6 Temperature dependent linear thermal expansion coefficients predicted by various models for UO_2	42
Figure 3.7 Temperature dependent isochoric heat capacities predicted by various models for UO_2	43
Figure 3.8 Temperature dependent isobaric heat capacities predicted by various models for UO_2	43

Figure 4.1 The connection of Yacub-09 potential and ZBL potential	47
Figure 4.2 Snapshots of a damage cascade initialed by the a 3 keV PKA in the $\Sigma 5$ (012)[100] system; the GB is between the two dashed lines	49
Figure 4.3 Numerical analysis of defects in the 3 keV damage cascade in bicrystal and monocrystal systems. The embeded figure shows the profile of different types of defects in grains of the bicrystal system	51
Figure 4.4 $\Sigma 5$ GB structure changes during the damage cascade. (a) is the structure before damage cascade; (b-g) are the evolution of the GB; (e-g) are the defects analysis corresponding to (b-d)	52
Figure 4.5 Snapshots of the damage cascade initialed by the 3 keV PKA in a UO_2 monocrystal system	53
Figure 4.6 Snapshots of the damage cascade initialed by the 1.5 keV PKA in the $\Sigma 5$ (012)[100] system; the GB is between the two dashed lines	54
Figure 4.7 Snapshots of the damage cascade initialed by the 1.5 keV PKA in the UO_2 monocrystal system	55
Figure 4.8 Numerical analysis of defects of the damage cascades initialed by the 1.5 keV PKAs in UO_2 bicrystal and monocrystal systems	56
Figure 4.9 The evolution of GB energies during the damage cascade for direct and indirect GB-cascade interactions in UO_2 bycrystal systems	59
Figure 5.1 The atomic potential energy in reference to the bulk of a $\Sigma 9$ (5 4 2)/(4 5 2) bicrystal system	62
Figure 5.2 The multiple layer structure of the simulation box for the Müller-Plathe method	63
Figure 5.3 The evolution of heat flux during of the Müller-Plathe method simulation. Red points refer to the bulk; black points refer to the $\Sigma 5$ (0 1 2)[1 1 0] GB; and blue points refer to the $\Sigma 9$ (5 4 2)/(4 5 2) GB	64
Figure 5.4 Temperature profile of UO_2 in bulk, $\Sigma 5$ (0 1 2)[1 0 0] and $\Sigma 9$ (5 4 2)/(4 5 2) bicrystal systems	65
Figure 5.5 Comparison of the GB energy of our work with Van Brutzel's [28]	67

Figure 5.6 Atomic configurations and energies [$\phi_{rij}-\phi_B$] of UO_2 containing a $\Sigma 5$ (0 1 2)[1 0 0] grain boundary before introducing a damage cascade, after quenching of a damage cascade, and after post-damage-cascade annealing, respectively.....	70
Figure 5.7 A plot of GB Kapitza resistances vs. GB energies for various configurations with or without radiation damage. The dash line refers to our fitting model	72
Figure 5.8 A plot of GB Kapitza lengths vs. GB energies for various configurations with or without radiation damage. The dash line refers to our fitting model	73
Figure 5.9 The correlation between the Kapitza length and the Kapitza resistance	73

LIST OF TABLES

	Page
Table 3.1 Size dependent melting temperatures of UO_2 predicted by different models..	42
Table 4.1 Transition regions for different ion-pairs.	47
Table 4.2 Damage cascade simulations in bicrystal UO_2 systems	57
Table 5.1 The Kapitza resistance, Kapitza length and energy of different CSL boundaries.....	67
Table 5.2 The Kapitza resistance, Kapitza length and energy of defects loaded GBs	71

1. INTRODUCTION TO FUEL MATERIALS

In traditional nuclear reactors, the release of nuclear binding energy by fissions of heavy isotopes in the fissile materials creates localized heating in the fuel element, which is transferred to a coolant, and then be used to produce mechanical energy and ultimately electricity. Understanding the properties and behaviors of these fissile material compounds is very significant in reactor safety and productivity. Based on their chemical compounds and states, the most common nuclear materials can be categorized into four types: oxide fuel, ceramic fuel, metal fuel and liquid fuel. Each type of fuel has their own pros and cons, as well as different applications to different types of reactors. Here we present an overview of nuclear materials, focusing on their degradation issues: section 1.1 is for oxide fuel; section 1.2 is for ceramic fuel; section 1.3 is for metal fuel; and section 1.4 is for liquid fuel.

1.1 Oxide fuels

Oxide fuel is one of the most well studied fuels. And uranium dioxide (UO_2) is the most frequently used and one among them. It has been widely used in light-water and heavy-water reactors. The massive application of UO_2 is not of no reason: being already in oxidized state, UO_2 is more chemical stable and inert, which ensure its compatibility with the coolant; UO_2 also has a higher melting point compared to metal fuels, and does not undergo phase transformation before melting; the irradiation stability of UO_2 is also good due to its CaF_2 crystal lattice [1].

The degradation issues have been paid attention to ever since the birth of Chicago Pile 1, which lumped metal uranium and uranium oxide together as the fuel, the degradation issues of uranium oxide has been studied. As shown in Fig. 1.1, high burnups lead to cracking as well as property changes in the fuel [2]. Besides influencing the heat transfer [1], expansion of fuel pellets due to crack formation puts stresses on the cladding, fractures the cladding, causing depressurization and loss of particulate, which increases the risk of fission products release during an accident [2].

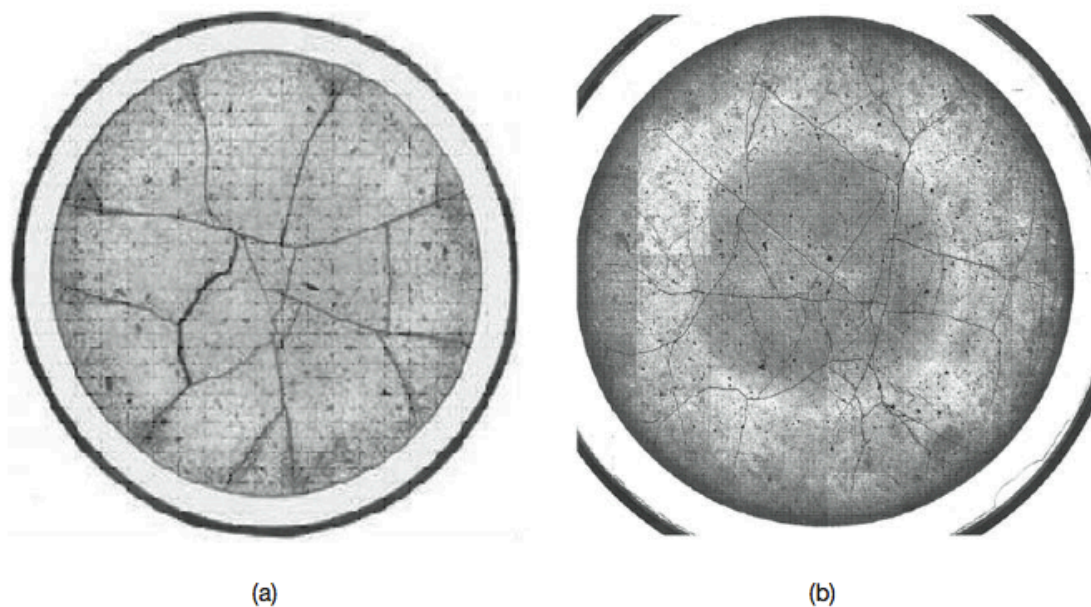


Figure 1.1: PWR cross section views of (a) Surry fuel at 35 GW•d/t U and (b) Robinson fuel at 67 GW•d/t U [2]

A more delicate look into the fuel structure will reveal the grain growth of the fuel, which takes place in the center of LWR fuel rods. As shown in Fig. 1.2, high temperature at the center of the fuel exaggerates irradiation enhanced grain growth. The growth is dramatic, following an empirical cubic relationship:

$$D^3 - D_0^3 = kt,$$

where D is the average grain size at time t , D_0 is the initial average grain size, and k is a temperature dependent factor [1]. The grain boundaries (GBs) trap fission gases and provide a place for bubble formation. Along GBs, fission gases and volatile products find a way to be released to the gap between the fuel and the cladding, thus, they could be more readily released during a cladding breach or other accidents [2].

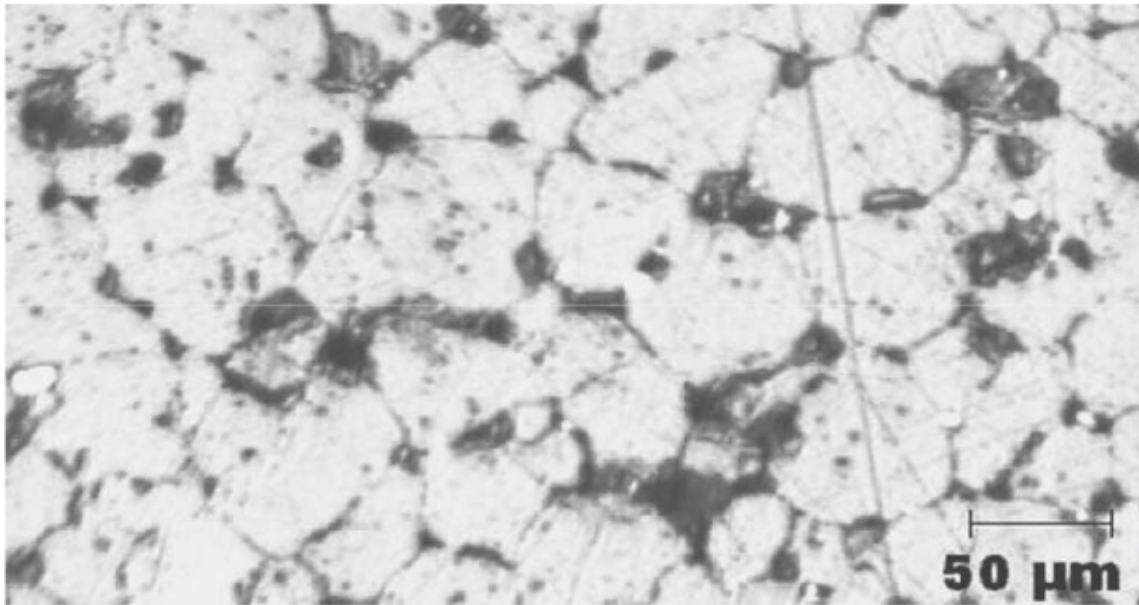


Figure 1.2: The center of a pellet of Robinson fuel at 67 GW•d/t U [2]

As discussed above, the volume of a fuel is of great impact to the safety of reactor operation. The volume change due to burning-up is mainly controlled by two mechanisms: fuel densification and gas swelling [3]. Speaking of the fuel densification, we have to mention that pores whose size and distribution are governed by the process of fuel pellets sintering from UO_2 powders [4]. The importance of the porosity is that the shrinkage of pores during operation affects the dimensional stability of the pellets. And

this process is called densification. Six factors have most impact on densification, those are: level of burnup, temperature, density, initial distribution of pore size, grain size, and O/U ratio [5]. And among them, the initial distribution of pore size determines the densification rate [5]. The mechanism of densification contains two processes: firstly, excess vacancies are generated near the pores by fission spike pore interaction, and then some of them immigrated to GBs and get annihilated [5]. On the other hand, As a result of reaction, fission products, including rare gases, are brought into the fuel material. Those products, especially rare gas bubbles, cause swelling of the fuel. Researchers have shown that neither gaseous fission products that in solid solution or in small intragranular gas bubbles, nor solid fission products makes important contribution [6, 7] to swelling. And the most significant contribution to swelling comes from the bigger intergranular gas bubbles [8]. And we can see that the level of burnup, temperature, density, pore size distribution and grain size are also the factors govern the swelling process. As a result from the densification and swelling, the volume of UO_2 fuel changes as shown in Fig. 1.3. The fast shrinkage of fine pores leads to a sharp decrease of the volume at the very beginning, followed by a moderated densification taking charge until a level of high burnup is reached, the swelling effect results in an asymptotical behavior eventually [5].

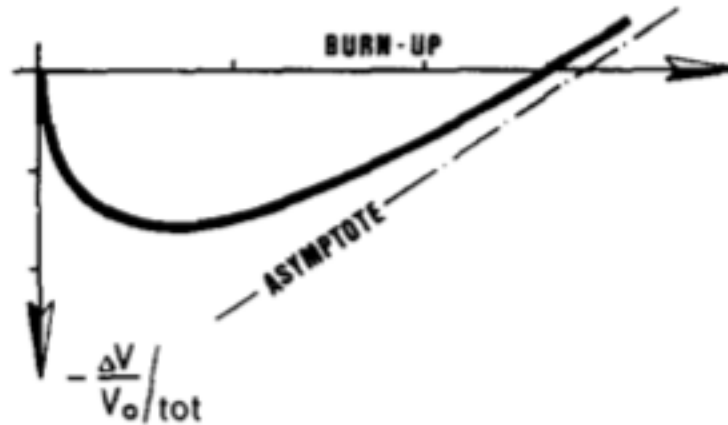


Figure 1.3: A typical in-reactor volume change of fuel pellets [5]

Another phenomenon referred as “rim effect” is very significant at high burnup fuels (above ~ 45 GWd/tU), in which a porous outer ring of 100-200 μm is formed. In the region of the ring, the higher neutron resonance absorption cross-section leads to the formation of plutonium; as a result of the presence of plutonium, local burnups at the rim region are greatly increased [9]. With a high damage level and inert gases content, heavily stressed grains subdivide into very fine grains. And fractures occur in these grains at high fission gas concentrations [10]. As a result, a “cauliflower” structure as shown in Fig. 1.4 is formed in the porous zone. This effect is very critical to the evolution of the fuel: the reduction of thermal conductivity brought by the porosity in the rim, serving as a barrier for heat flow, leads a significant increase to the temperature at the center of the fuel [10].

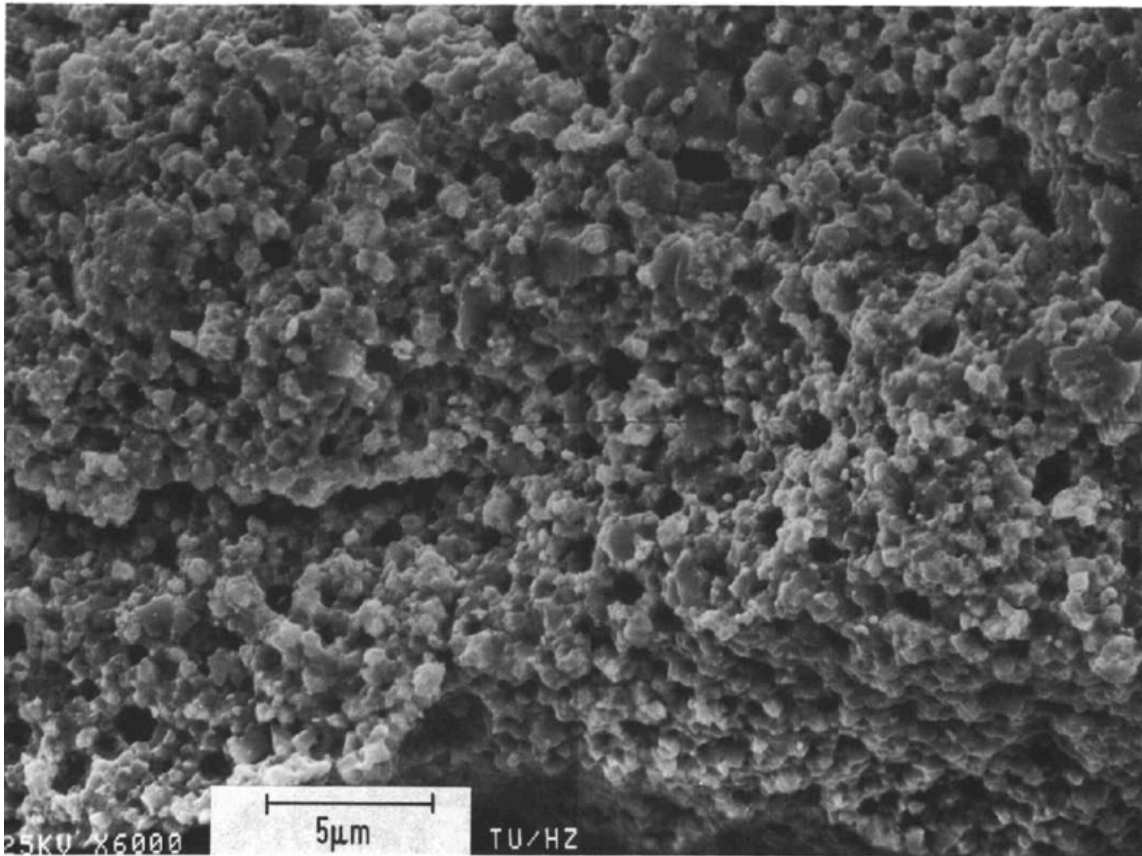


Figure 1.4: The porous structure formed in high burnup UO_2 fuel [11]

1.2 Ceramic fuels

Compared to oxide fuels, ceramic fuels such as uranium nitride and uranium carbide have a higher uranium density, higher thermal conductivity, higher melting point and stronger resistance to creep under neutron irradiation [12]. Due to their chemical similarity, degradation issues in oxide fuels are also challenging ceramic fuels.

Uranium carbide has been studied as a promising fuel material for gas-cooled fast reactor. And one issue of the application is the fuel/cladding interaction. The cladding acts as a sink for carbon and decarburizes the fuel, making the fuel fragile; on

the other hand, the carburized cladding also suffer from the loss of ductility [13]. Due to the issues caused by the compatibility of uranium carbide with stainless steel cladding, understanding the volume change becomes significant. It has been shown that under ~ 970 K and burnups less than 5×10^{20} fissions/cm³, it is unlikely for bubbles to form [14] and the main contribution to the swelling of the fuel comes from condensed phases of fission products, which are dominated by ternary compounds like UMoC₂ and U₂RuC₂ and carbides of fission product elements [15]. As shown in Fig. 1.5, the volume of the fuel is almost proportional to the level of burnup. And the ratio of uranium to carbon influences the swelling of fuel [15]. As for the role of gases at higher burnups and higher temperatures, simulation based on the homogeneous nucleation theory has made prediction that ally with experimental data very well, as shown in Fig. 1.6 [14].

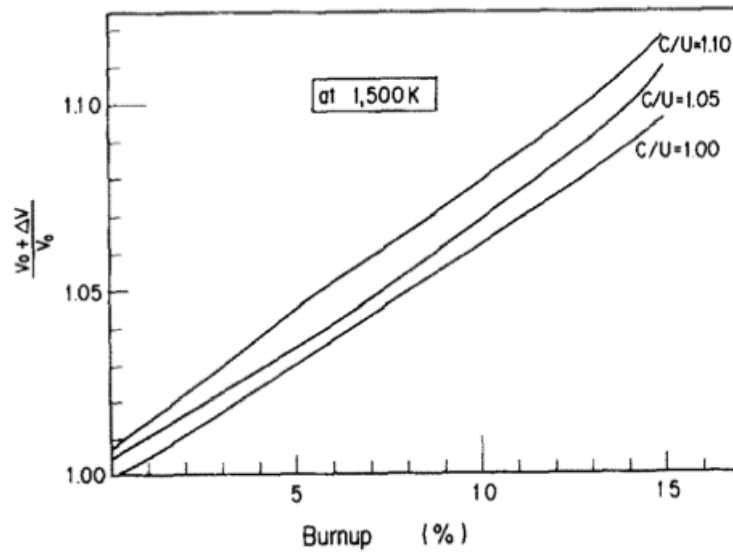


Figure 1.5: Volume increasing rates of uranium carbide fuels caused by solid fission products [15]

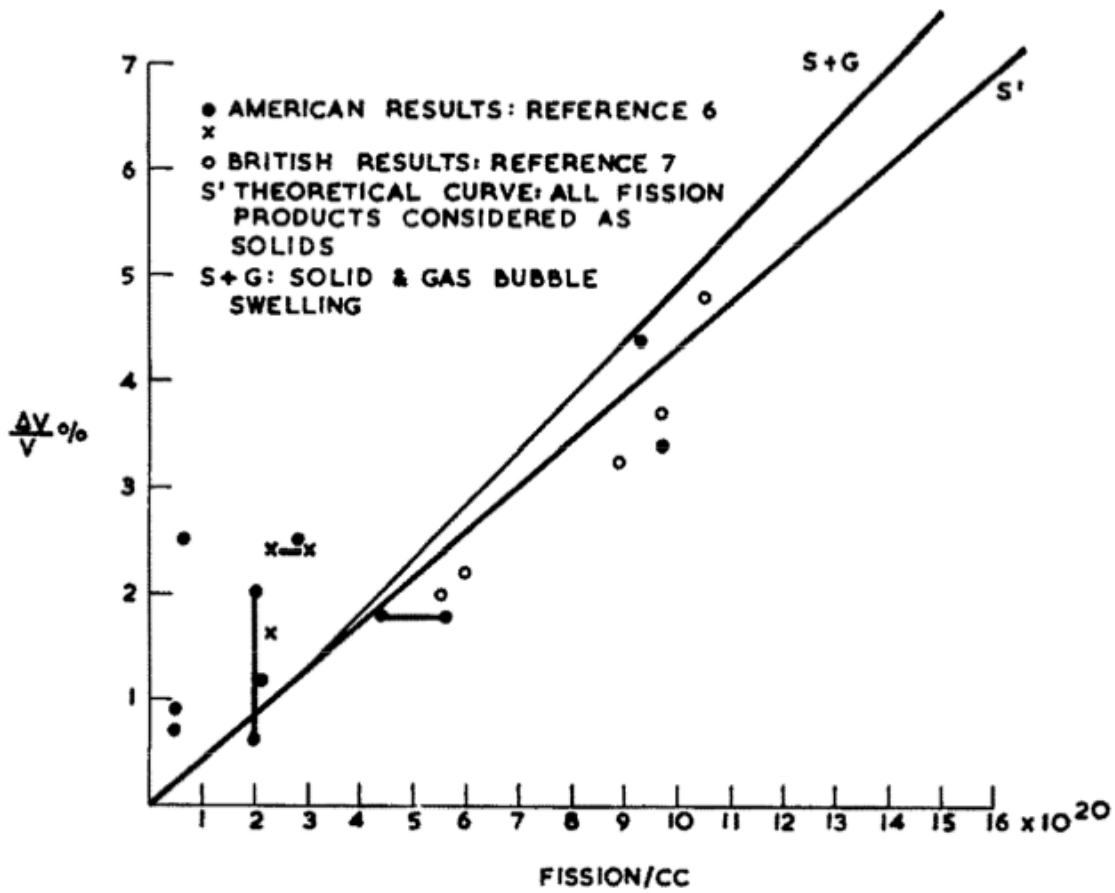


Figure 1.6: A comparison of theoretical predicted and experimental measurement of the uranium carbide swelling [14]

Another common type of ceramic fuel is uranium mononitride, which has desirable properties as a fuel material, such as its face-centered cubic structure, the high melting point, high thermal conductivity, high uranium density and high irradiation tolerance. However, the disadvantage of the parasitic capture of neutrons in the transmutation of nitrogen atoms is also significant [13]. And another practical disadvantage is that the nitrogen required to produce uranium mononitride fuel is very expensive.

1.3 Metallic fuels

The metallic fuel is the earliest proposed potential type of fuel for fast reactors, for the “extremely hard neutron spectrum” it provided [16]. Unlike oxide fuel or ceramic fuel, metallic fuel has a relatively poor radiation tolerance. As a result, generally, the operation temperature is limited up to $\sim 873\text{K}$ and burnup level is limited up to $\sim 5\text{MWd/kg U}$. Actually even this operation temperature and burnup level are too high to achieve without adding other elements into uranium-plutonium alloy. Although chromium, molybdenum, titanium also increase the melting point of the alloy adequately [16], zirconium is outstanding because it suppresses the interdiffusion of fuel and cladding components [17].

Even at low temperatures, lattice defects such as vacancies, interstitials and dislocation loops form significantly under irradiation. Together with the formation of fission gas bubbles at high temperatures, it brings in serious swelling and growth issues [13]. Fig.1.7 illustrates the axial growth during fuel burning up. In addition, anisotropic swelling has been found as a result of the difference in swelling behavior between the colder periphery of the fuel and the center [18]. Usually, the diameter of the fuel can expand up to 15% and reach the cladding, compared with the axial growth of 2% to 8% as shown in Fig.1.7.

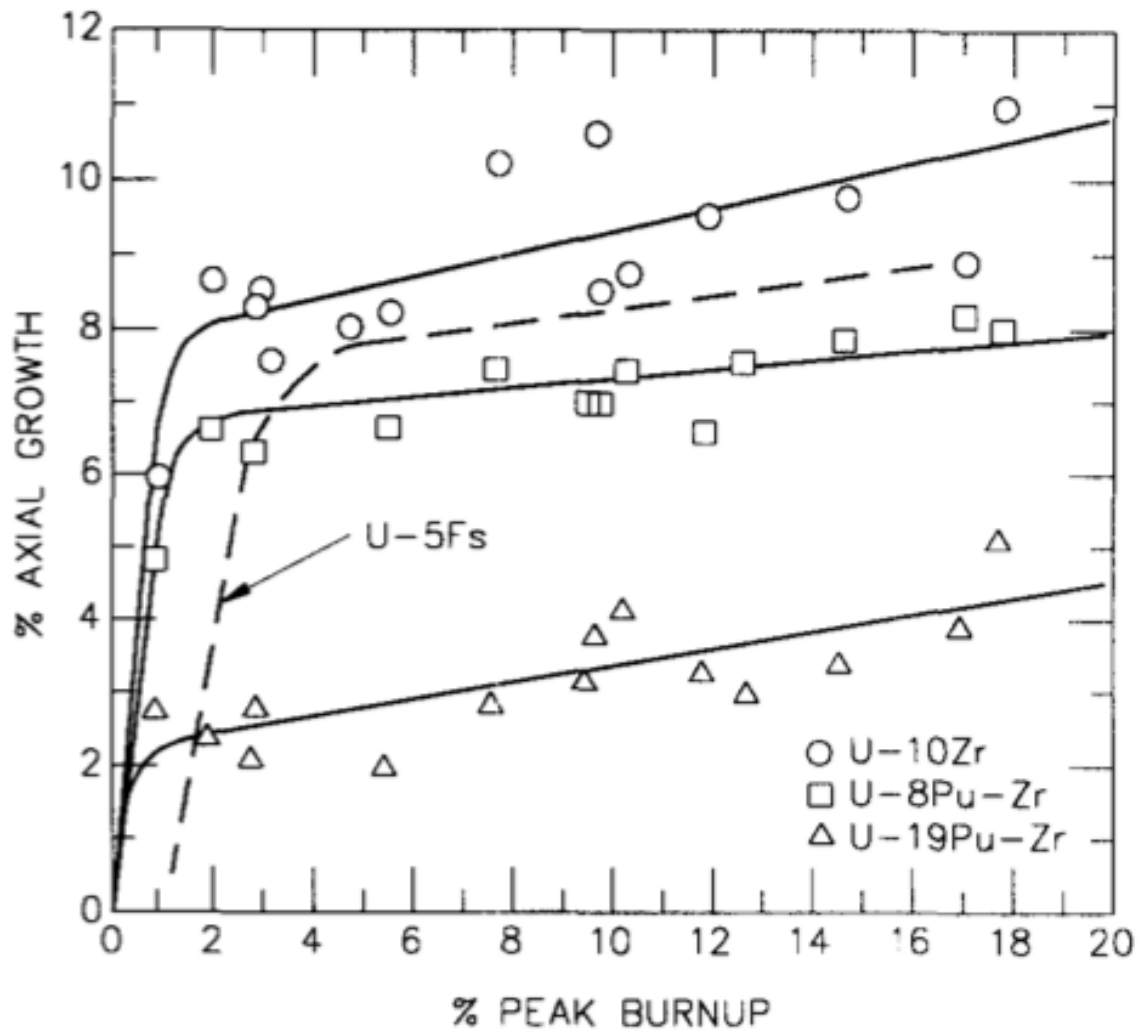


Figure 1.7: The increase of the length of various metallic fuels as a function of burnup level [16]

As the fuel expands to reach the cladding, the fuel cladding interaction begins to draw attention. The first thing is the fuel/cladding mechanical interaction. This phenomenon is very serious in early designed reactors since they do not have enough spaces for the swelling of fuels; as a result, the pressure from gas-bubbles in the fuel is directly transmitted to the cladding. And that is why cladding deformation and rupture

occur at as early as modest burnups in early designs [16]. The challenges of fuel/cladding mechanical interaction serve as a driving force for the study of cladding deformation behaviors, and more deformation resistant materials have been developed and applied in reactors. As shown in Fig.1.8, new stainless steel like HT9 has been developed to have very low deformation even at a relatively high burnup level. On the other hand, the touch of the fuel and the cladding greatly enhances fuel/cladding chemical interaction (FCCI). The direct result of FCCI is that it thins the cladding and produces new phases that have undesirable properties such as a lower thermal conductivity or a lower ductility [19]. Due to the complexity of the chemical components of both the fuel and the cladding, the intermetallic phase formation can be very complicated, especially for the case under irradiation. To study FCCI, diffusion couples of fuel material and cladding material have been made since 1960s. For example as shown in Fig.1.9, in a recent study, diffusion couples of uranium and iron have been annealed at different temperatures to study the mechanism and kinetic of intermetallic phase formation [19]. One important fission product that impacts FCCI is lanthanide, which influences the interdiffusion process. Researchers have found that FCCI is determined by the particular fuel/cladding combination and temperature before lanthanide accumulated at the interface; but dominated by the presence of lanthanides after there is enough of them. And the accumulation of lanthanide at the interphase is influenced by the burnup level, the temperature and the fuel alloy type [16].

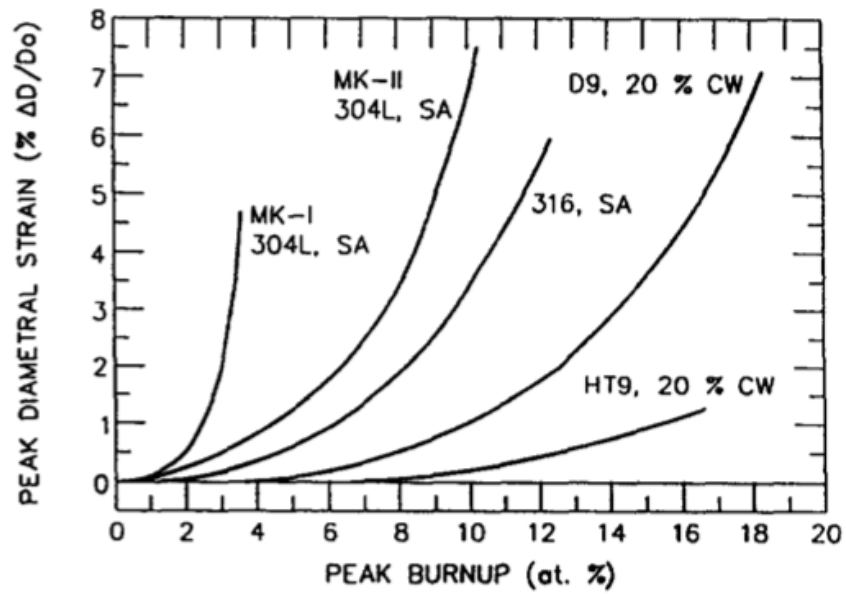


Figure 1.8: The progressive improvement in the deformation of the cladding of metallic fuel elements [16]

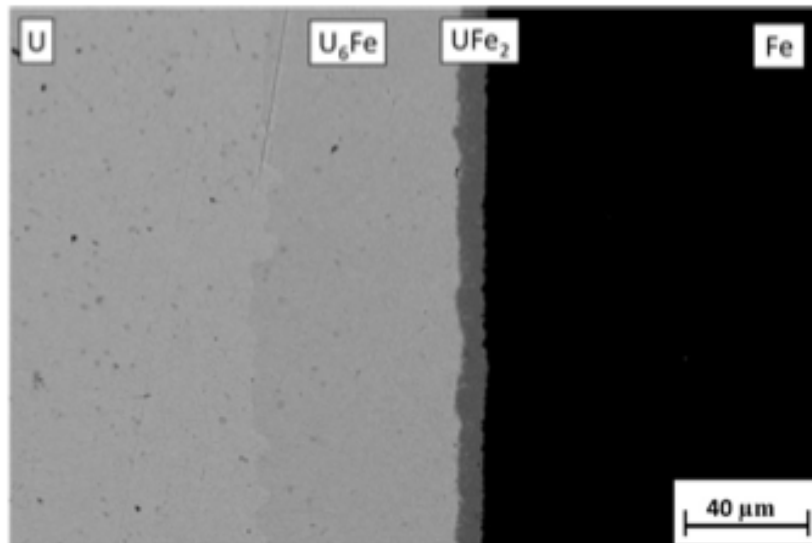


Figure 1.9: A diffusion couple of uranium and iron showing formation of intermetallic phases [19]

1.4 Liquid fuels

Being in different state, a liquid fuel is very unique compared to the other types of fuel introduced above. One benefit of liquid fuels over solid fuels is that it has stronger negative feedback due to the higher level of thermal expansion, due to the nature of liquid. This increases the stability of the reactor designs. Also a liquid fuel has a higher chemical flexibility, a higher thermal conductivity and a better radiation resistance [20]. However, as every coin has two sides, the nature of liquid also makes it more easily dispersible in the case of an accident.

The molten salts fuel is one main type of liquid fuel. One significant different from the solid fuel is that the molten salts fuel does not has a separated coolant; the nuclear fuel is dissolved in the coolant itself. This quite simplifies the system but there are mainly three difficulties in building a molten salts reactor: the corrosion resistance of the structural metal should be improved to stand the attack from the fuel; a liquid fuel requires higher fuel concentration for criticality, which means the power output per unit mass of the fuel is relatively low; and because of the high melting point of the salts, heating up the system to above the melting point of the salts provides additional difficulties [20]. In spite of these difficulties, the advantages of liquid fuel reactor are still driving more and more researches for it.

These four types of fuels dominate in past and current reactor designs. And in our work, we will focus on the UO_2 fuel, which has been intensively studied and is still drawing huge amount of interests from current researchers.

2. PREVIOUS RESEARCH IN UO_2 SYSTEM

As we discussed in the first section, we noticed that almost all the safety issues we discussed are temperature related: cross-sections of materials are always a function of temperature; the process of defects formation and annealing is strongly influenced by temperature; high temperature increase the formation of cracks; temperature is one of the six factors that influence densification swelling processes; grain refining is more significant at high temperature zone; and interactions between fuel and cladding, for example interdiffusion, are also controlled by temperature. Motivated by the importance of temperature in fuel behaviors, researches on thermal properties of fuel materials are necessary and useful. In this section, we use UO_2 , one of the most well studied fuel material and one candidate fuel for Generation IV reactors, to show current studies on thermal properties of fuel materials. We start with some experimental work in section 2.1; then discuss simulation studies in monocrystal systems in section 2.2; followed by simulation studies focused on the role of GBs in thermal properties and radiation damage in section 2.3; then in section 2.4 we will present the motivation of our research.

2.1 Experimental studies on thermal properties of UO_2

Experimental studies of UO_2 provide a lot of direct measurements of important properties, which serves as important references for reactor design and modeling. From earlier studies we know that different mechanisms for the thermal conductance dominate

in different temperature regions. As shown in Fig. 2.1, the thermal conductivity decreases with the increasing temperature at lower temperature region, reaches minimal value at around 1900K and then increases at higher temperatures. The characteristic decrease of thermal conductivity before 1900K is due to the increased incidence of lattice phonon scattering; and the reason of the significant increase afterwards is due to electronic process like electrons and holes motilities [21].

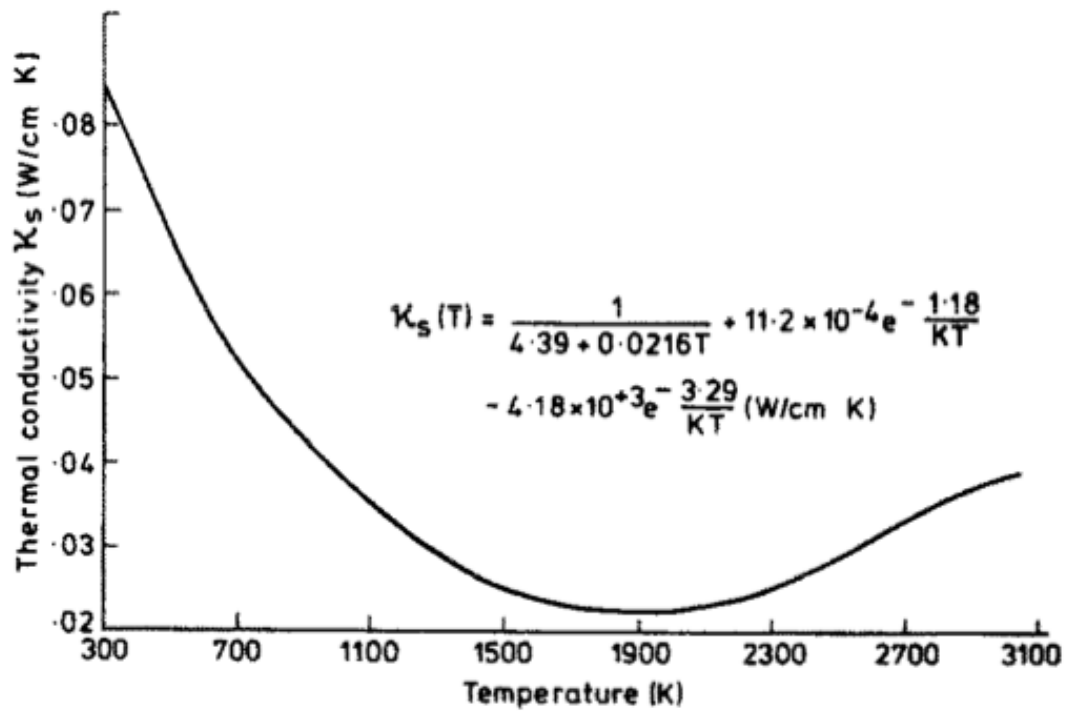


Figure 2.1: The thermal conductivity of UO_2 as a function on temperature [22]

Generally, the operation temperature of most types of reactors is below 1500K. As shown in Fig. 2.2, experimental data in the low temperature region ally with theoretical calculation based on phonon transportation very well, showing strong evidence that at temperature of nuclear reactor operation, thermal conductivity of UO_2 is

basically governed by phonon transportation, and phonon scattering serves as a main source of thermal resistance. Fig. 2.3 shows that both higher O/U ratios and higher temperatures lead to lower thermal conductivities. That is because excess oxygen ions serve as a phonon scattering center for the case of higher O/U ratio; and higher temperature leads to more phonon-phonon scattering.

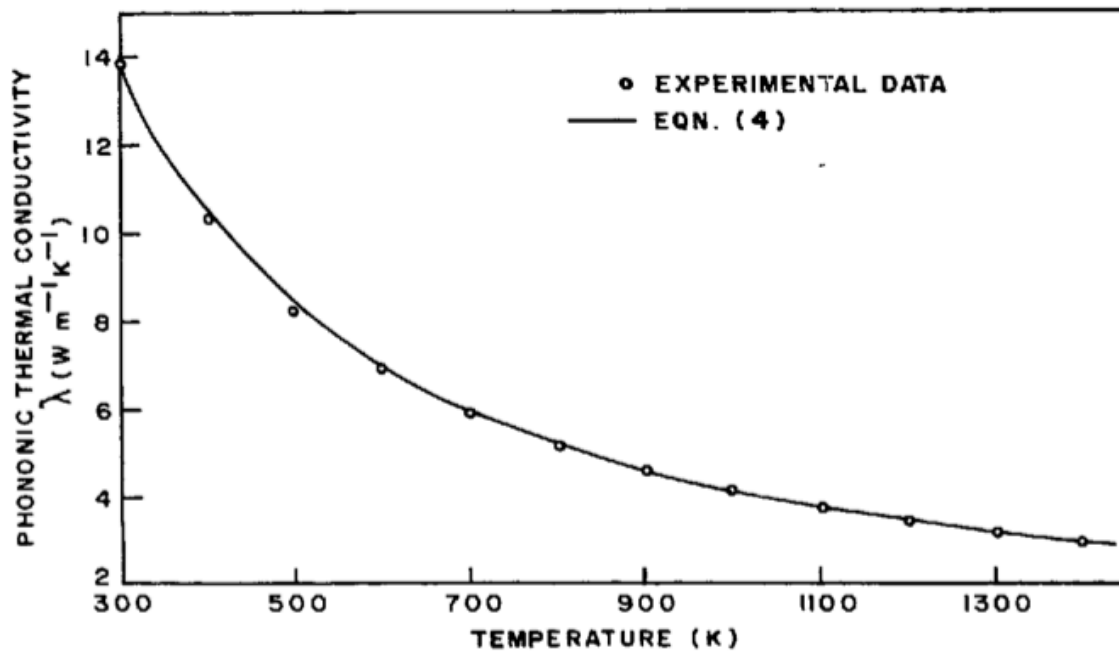


Figure 2.2: The phonon thermal conductivity of UO_2 obtained from experiment compared to that computed using modified Leibfried-Schlomann equation [23]

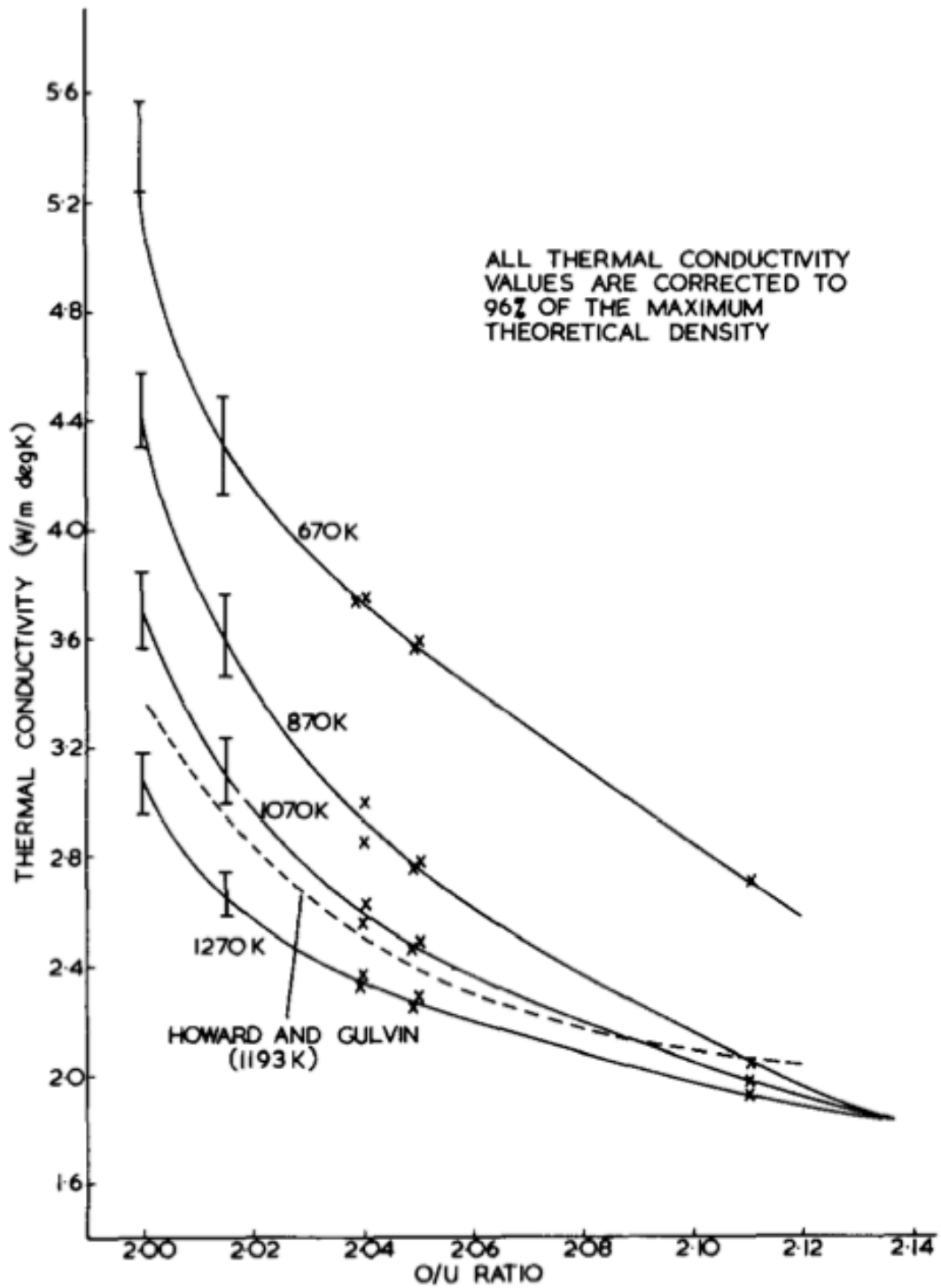


Figure 2.3: The thermal conductivity of UO_2 as a function of O/U ratio at different temperatures [24]

While the monocrystal has a relative simple mechanism of phonon scattering, the presence of GBs provides a challenge. In section 1 we can see that GBs are very important in the behavior of reactor fuels: they are sinks for defects; they influence the densification and gas swelling significantly; and the distribution of GBs varies in different regions of the fuel: in the center of the fuel due to high temperature there is less larger grains and thus less presence of GBs; and in the periphery region, as the result of rim effect, there is a very dense distribution of GBs. Researches on the structure and distribution of different GBs [25], the role of GBs on gas release [26], the effect of GBs on the damage cascade evolution [27, 28], et.al have been carried out in the past.

The nature of GBs is very complex; while simulation studies provide more details like structures and subtle mechanisms, experimental researches give us general ideas on what GBs are and how they influence the properties of materials. Fig. 2.4 shows the scanning electron microscopy (SEM) and electron backscatter diffraction (EBSD) measurements of a UO_2 sample, and length distribution of GBs on misorientation angles and coincident site lattice (CSL) [25]. It was observed that the distribution of GBs on misorientation angles is close to random distribution representing the Mackenzie distribution for a cubic crystal [29], but slightly more highly distributed around 42° [25], suggesting that there may be a weak influence of the GB itself (i.e. the GB energy) on this distribution. They also reported that about 16% of the GBs are CSL boundaries, and $\Sigma 9$ GB dominates the distribution of CSL boundaries, as shown in Fig. 2.4(c) [25].

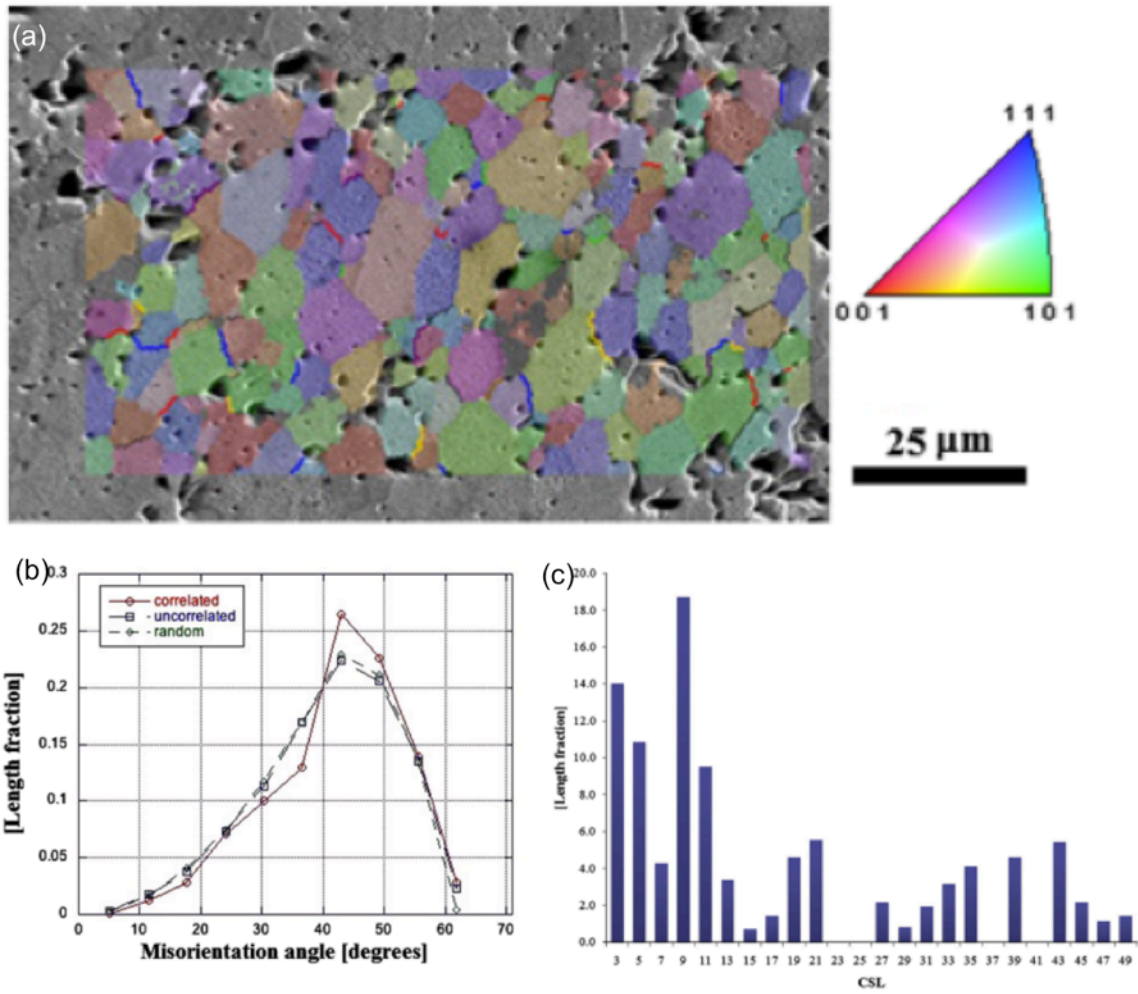


Figure 2.4: Experimental characterizations of GBs in a UO_2 sample: (a) The SEM and EBSD image of the sample; (b) the length distribution of GB on misorientation angle; and (c) the length distribution on CSL boundaries [25]

Figure 2.5 illustrates the effect of GB as a phonon scattering center [30]. Similar to the interface of two solids as shown in Fig. 2.5, GBs will provide a resistance to the heat flow across them, leading to a temperature gap if a stable temperature difference is applied between the two ends of the system. The thermal resistance at a GB/interface is called the Kapitza resistance and defined by the temperature drop at the GB/interface over the heat flux through the GB/interface. However, under most conditions, the

temperature drop cannot be accurately measured in experiments, due to the background noise. An equivalent value to a Kapitza resistance is the Kapitza length, which is defined as the produce of the Kapitza resistance and the thermal conductivity of solid 1 as shown in Fig. 2.5. In experiments, a heat source is set on one side of the GB and a probe is set on the other side. The temperature of the heat source is set to be sinusoidal with time, and the frequency is specified so that the “temperature wave” can penetrate deep enough into the sample, to avoid the surface effect. The probe sitting on the other side of the GB will detect the “temperature wave” and the phase delay due to the presence of the GB can be measured. And thus the Kapitza length can be directly derived from the phase delay. This method is employed in researches nowadays on the effect of GBs in UO_2 fuel systems.

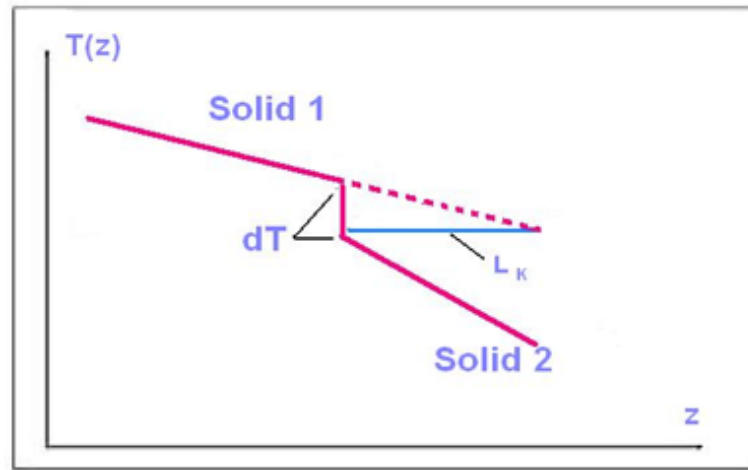


Figure 2.5: A schematic diagram for the interface thermal resistance (known as the Kapitza resistance) and the Kapitza length [30]

2.2 Simulation studies on thermal properties of monocrystal UO_2

As a result of the fast development of computing ability, simulation studies play more and more important roles in understanding the mechanisms of experimental phenomena. For researches on thermal properties, molecular dynamics (MD) simulation is a very powerful tool. A detailed introduction to this simulation method will be provided in section 3. In this part we present some interesting findings from recent researches, to review our current knowledge of the thermal properties of UO_2 fuel systems.

MD simulations predict thermal properties of UO_2 systems very well, as shown in Fig. 2.6 [31]. For the four properties investigated in Yamada's work, i.e., the lattice parameter as shown in Fig. 2.6 (a), which actually reveals the thermal expansion, the specific heat as shown in Fig. 2.6 (b), the thermal conductivity as shown in Fig. 2.6 (c), and the compressibility as shown in Fig. 2.6 (d), they all reasonably agree with experimental results. That is not surprising because MD simulations are based on classical interaction between atoms, which is the basement of theories of phonon. It is worth to point out that at around 2200K, Fig. 2.6 (b) and Fig. 2.6 (d) show some jump like features in the specific heat and compressibility. As reported by Yamada et.al, this comes from the "Bredig" transition, which is an anion diffusive transition occurred at high temperature. The "Bredig" transition increases the soft and creep rate of UO_2 , leading to a high compressibility; and the peak in specific heat shown in Fig. 2.6 (b) is the result of the onset of superionic conduction [31]. Figure 2.7 shows direct evidence of the "Bredig" transition [31]. We can see that the system remains solid due to the crystal

structure of uranium atoms; on the other hand, oxygen atoms begin to diffuse at high temperatures, meanwhile, their mean square displacements become very large.

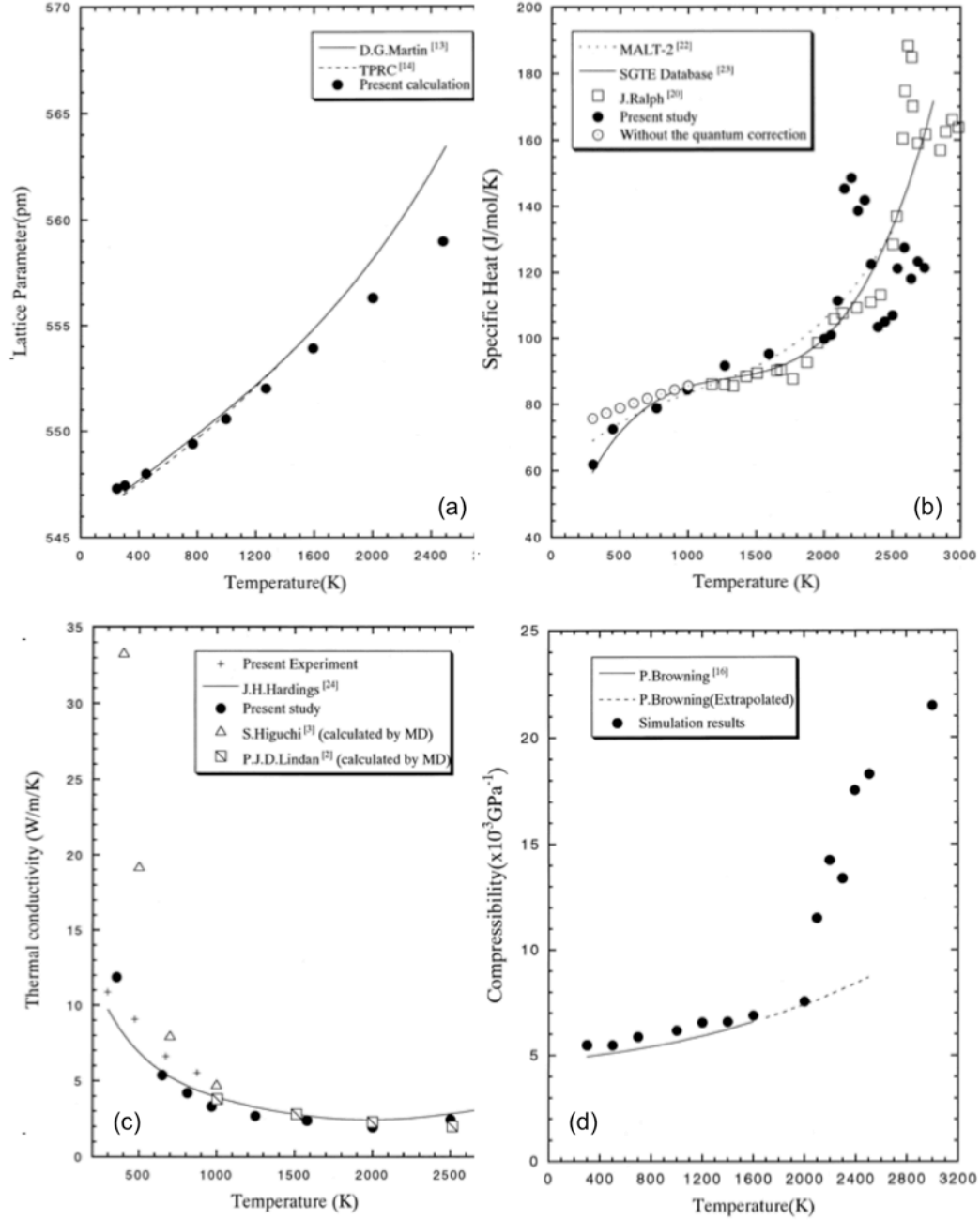


Figure 2.6: Thermal properties calculated from MD simulations compared with experimental data [31]

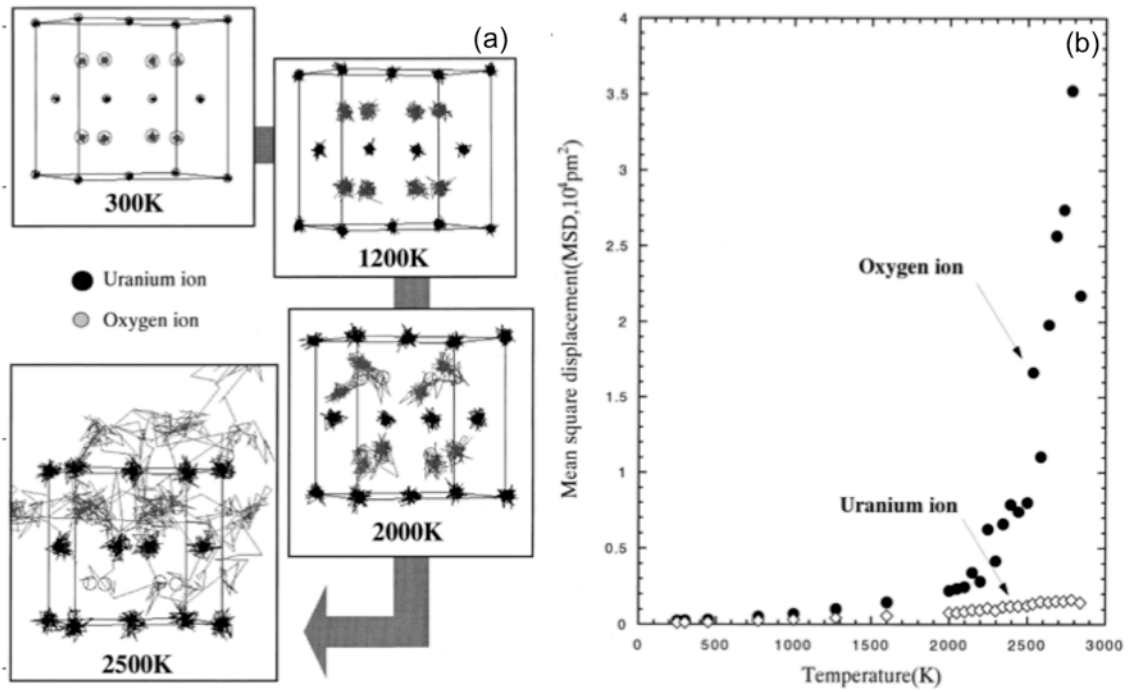


Figure 2.7: The “Bredig” transition in MD simulations: (a) a track of atoms with increasing temperatures; (b) mean square displacements of uranium and oxygen atoms as a function of temperature [31]

Influences of other conditions besides the temperature to thermal properties of UO₂ were also studied through MD simulation. For example a recent study on the influence of non-stoichiometry and oxygen Frenkel pairs on the thermal conductivity shows good agreement and very promising explanations to experimental data as we discussed in section 2.1 [32]. Non-stoichiometry always happens in nuclear fuel and is an issue of great practical values. As shown in Fig. 2.8, the off-stoichiometry suppresses the thermal conductivity. That is normal because both vacancies and interstitials serve as phonon scattering centers. On the other hand, a careful observation into Fig. 2.8 will find that even at the same absolute value of x , vacancy rich side ($x < 0$) has a lower thermal

conductivity then interstitial rich side ($x > 0$). According to Nichenko, et.al, the reason is that the presence of vacancies causes the absence of phonon carriers at these lattice positions [32]. To further study the effect from Frenkel pairs, they calculated the temperature dependent thermal conductivities of systems with initially different density of Frenkel pairs. The result shown in Fig.2.9 illustrates that higher temperature enhanced annihilation of Frenkel pairs, which compensates the decrease of the thermal conductivity due to the enhanced phonon-phonon scattering. However, as most of the Frenkel pairs are recombined after 900K, the thermal conductivity drops again as temperature continues to increase.

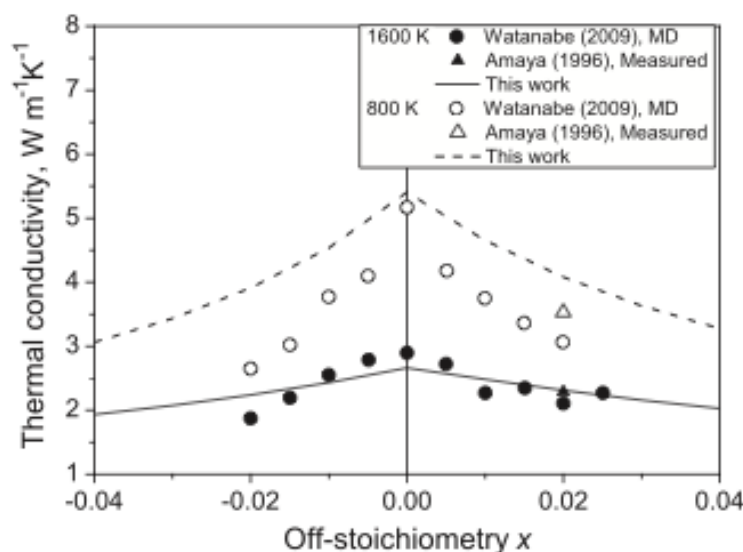


Figure 2.8: Comparison of experimental and simulation data of thermal conductivity at different temperatures of the non-stoichiometric UO_{2+x} as a function of x [32]

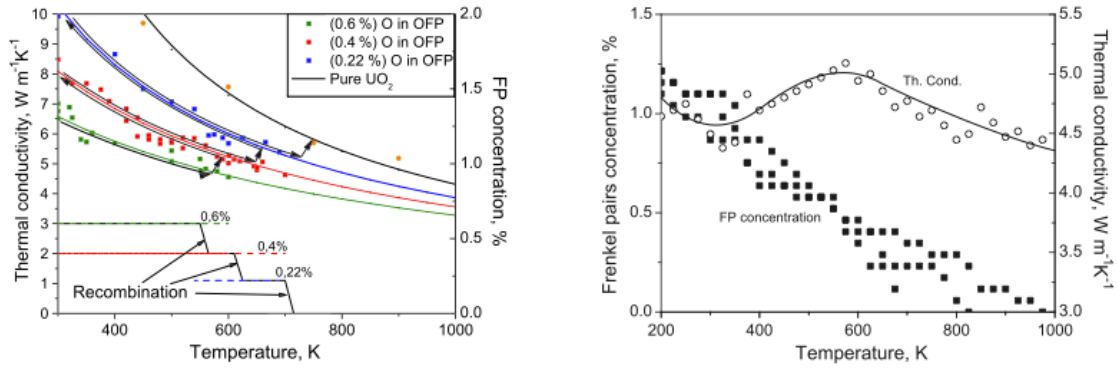


Figure. 2.9: Thermal conductivity recovery (left) and Frenkel pairs recovery (right) during annealing for UO₂ system [32]

2.3 Simulation studies focused on the presence of GBs

MD simulation has been shown as a very powerful tool in studies of GBs of UO₂ systems for different purposes [25, 27, 28, 33]. Here we present the work of Watanabe for the influence of GBs on thermal conductivities and works of Van Brutzel for the role of GBs in damage cascade evolutions.

By comparing the thermal conductivities of a series of artificial polycrystalline structures as shown in Fig.2.10 (a), Watanabe, et.al reported that the presence of GBs suppresses thermal conductivities to around one magnitude order lower than it in a monocrystal system[33]. This effect is more significant at lower temperature when phonon-phonon scattering is not significant, as shown in Fig. 2.10(b). Figure 2.10(c) shows the grain size dependent thermal conductivities of UO₂, giving a clear trend that finer grains have a stronger suppression on thermal conductivities of the UO₂ fuel. Hence, it is very important to have a more detailed understanding of the roles of GBs in thermal conductivities.

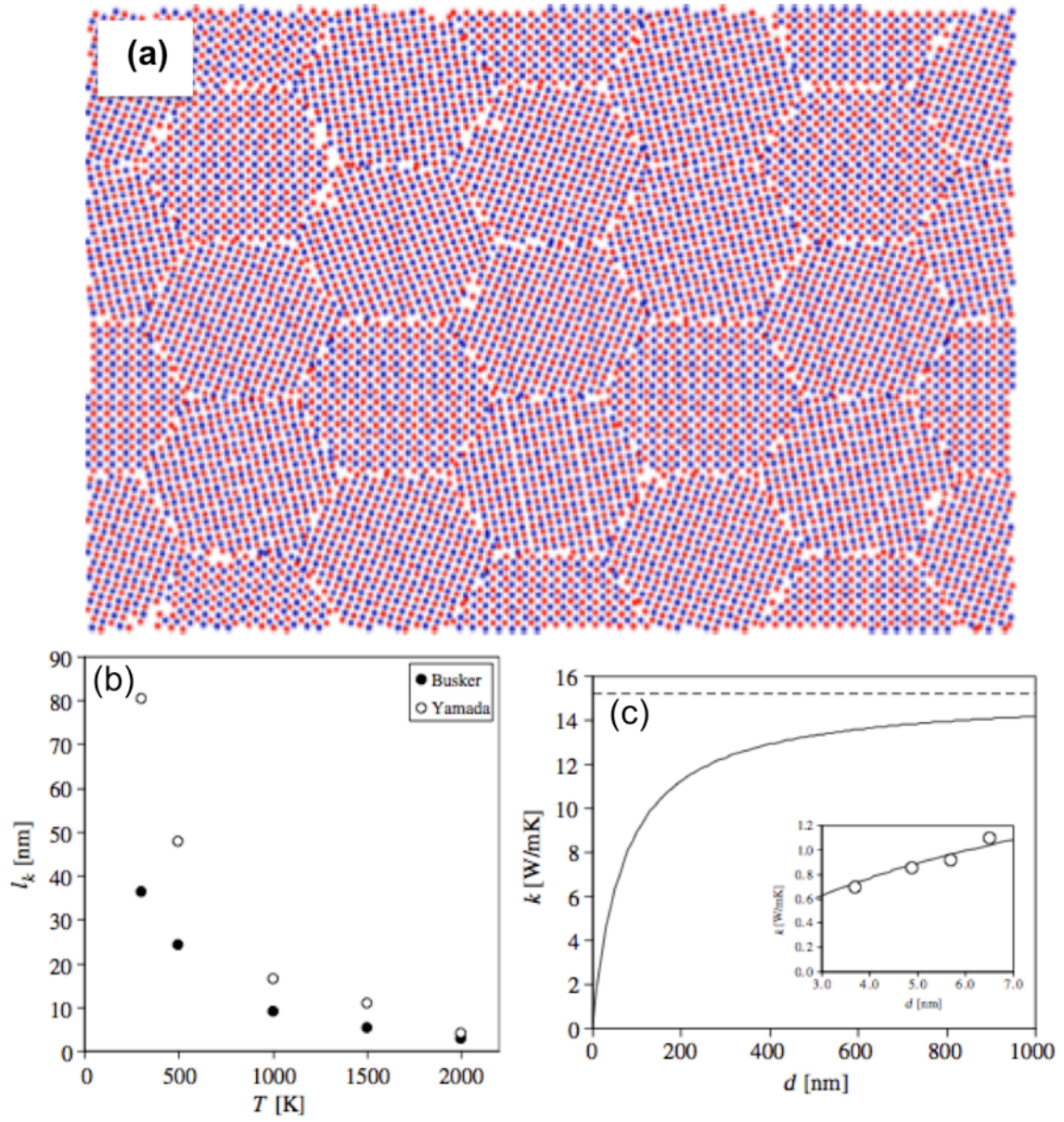


Figure 2.10: Simulation study of thermal conductivities of polycrystalline UO_2 : (a) the structure of polycrystalline UO_2 system; (b) the Kapitza length of 3.8 nm grain polycrystalline UO_2 calculated from different potentials; (c) grain size dependent thermal conductivity from Yamada potential [33]

It is well known that GBs serve as sinks to defects. Due to the fact that the reactor fuel is under an extreme irradiation environment, the interaction between GBs and defects is very influential to the behavior of the fuel. Van Brutzel et.al reported that the GBs do act as a sink to the low energetic atoms especially at the early stage of damage cascade [28]. They also found that different mismatch angles of symmetric-tilt GBs lead to different defect structure at the GBs, which later influence the evolution of damage cascade [27, 28]: as shown in Fig. 2.11, for GBs with vacancy defects at the interface, an asymmetric distribution of defects between the two halves of the bicrystal systems are found.

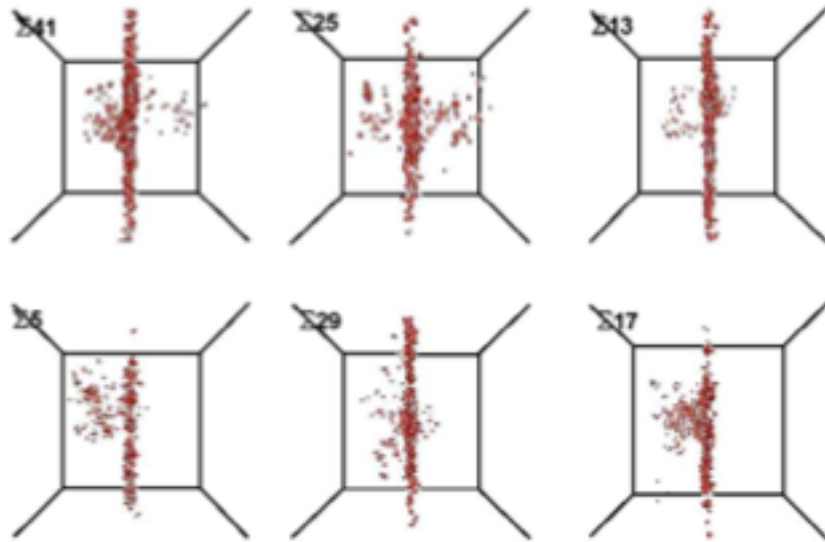


Figure 2.11: Spatial distribution of point defects in different CSL GBs after relaxation of displacement cascades [28]

2.4 The motivation of our research

As emphasized in Section 1, the role of GBs and their property changes under irradiation is very important in heat transfer in the fuel. While the case of monocrystal uranium oxide is relatively easier to describe, as shown in Section 2.2, the presence of GBs complicates the issues and brings more significant research topics. However, most of current modeling of heat transfer in reactors neglect or oversimplified the influence of GBs. As a result, a fundamental study that can provide with predictions of the behaviors of GBs is in great need to improve modeling of reactors. The work of Watanabe et.al [33] provides an overview of the influence of GBs on the thermal conductivity, but we still need more details focusing are different types of GBs, and GBs with defects loaded, since the fuel is exposed in irradiation environment. The works of Van Brutzel et.al [27, 28] focused on the influence of different types of GBs on damage cascade evolutions, but did not discuss enough on the evolutions of GBs themselves during the cascades. Thus, we are trying to find the missing pieces and our research will be composited by two parts: the evolution of GBs in UO_2 systems under irradiation; and the thermal resistance of GBs with different structures and different levels of defect loads.

Besides the benefit to reactor modeling, our research will make good contribution to experiments being carried out as described in Section 2.1, especially for the nanoscale measurements of direct contribution of GBs to the thermal conductance in UO_2 systems. Our simulation result will provide an important reference.

3. MOLECULAR DYNAMICS SIMULATION

Before presenting our work, we have in this section a detailed introduction to MD simulations for the reference of future sections. Section 3.1 introduces the concept of MD as well as the code we are using: large-scale atomic/molecular massively parallel simulator (LAMMPS); section 3.2 talks about the simulation of ion-solid interactions; section 3.3 emphasizes on MD simulation for thermal conductivity, conductance or resistance calculations; and section 3.4 provides an overview of interatomic potentials of UO_2 systems, as well as a brief introduce to the potential we choose for our work.

3.1 An introduction to MD simulations

The concept of MD simulations is not complex: with an interatomic potential governing the interaction between atoms through Newton's second law, the behavior and evolution of a system composited by a number of atoms are determined and computed given initial and boundary conditions. The calculation is realized by discretize the time into timesteps, and in each timestep, Newton's law based on interatomic potential works out the situations (position, energy, momentums, et.al) of all atoms in the next timestep based on the input of the situations of all atoms in the current timestep. This process is repeated over and over to simulate the evolution of the system in a given time period, as shown in Fig. 3.1 [34]. The discretization causes errors. To minimize the errors, usually the timestep is in the order of femtoseconds. Due to the limitation of computing abilities, the timescale of MD simulation is usually limited up to nanoseconds. Recently, coupling

of MD simulations and Monte Carlo simulations is being carried out to enlarge the timescale.

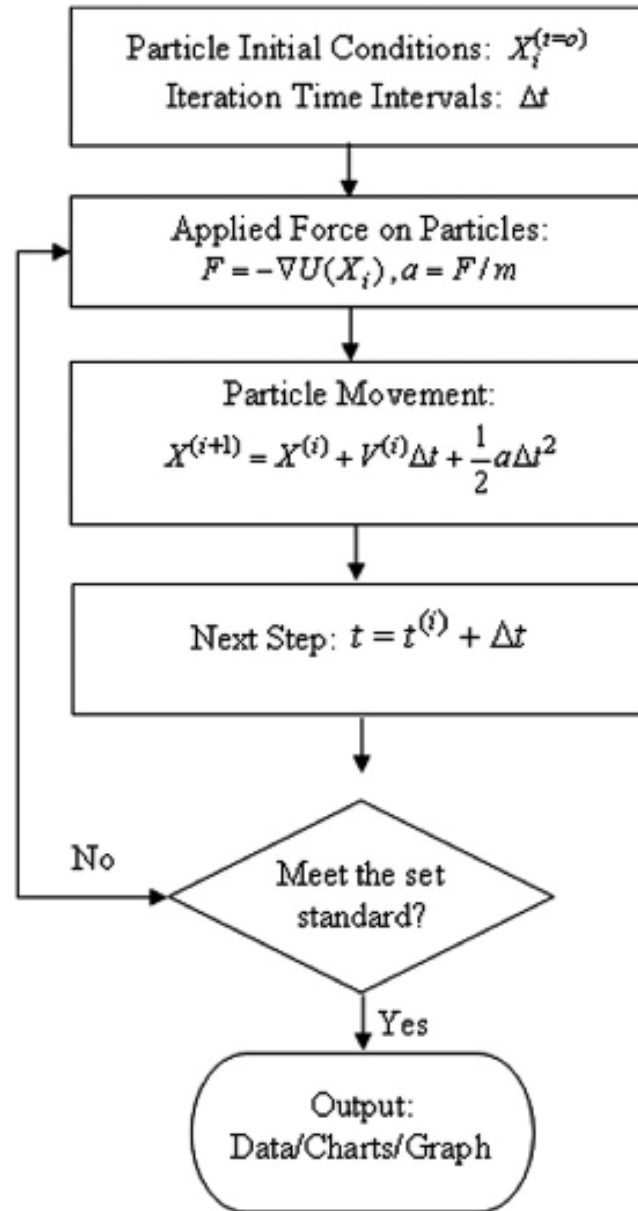


Figure 3.1: A sketch of the algorithm of MD simulations [34]

LAMMPS is an open source code distributed by Sandia National Laboratories [35]. Four basic features of it (actually for most MD simulation codes) are: point mass atoms, interactions between atoms described by simple forces, atomic positions and velocities advanced by Newton's second law, and thermodynamic statistics generated from the state of atoms [35]. The main advantages of LAMMPS are: it runs on both single and parallel processors; it builds as library and couples with other codes easily thanks to its open source; it supports most of interatomic potentials and most types of particles including atoms, polymers, organic molecules, proteins, metals, point dipolar particles, et.al. In addition, because both the interatomic potentials and atomic structures are loaded from text files into the simulation, there is huge space for custom potentials and systems. Any type of two-body interaction can be numerically described and input as a LAMMPS interatomic potential.

3.2 MD simulations of ion-solid interactions

Ion beam technologies have been widely used in many fields including materials characterization and modification, semiconductors produce, atomic and nuclear physics studies, medicine, biology, etc. By employing various elements with different energies, ion beam can be used to simulate different types of radiation damages that occur in reactors. Ion-solid interaction occurs when ion-beam is bombarded into solid materials. As shown in Fig. 3.2, ions interact with both electrons and atoms in the solid, and lose energy to them. The ability of materials to slow down the bombarding ions can be described by the stopping power, which is the average energy loss of the ion per unit

path length in the solid. The stopping power is material dependent and a function of the energy of ions. Figure 3.3 illustrates nuclear and electronic stopping powers as a function of ion energies [36]. Nuclear stopping corresponds to the process of ion loss energy through nuclear collisions, while electronic stopping corresponds to the process of ion loss energy to electrons. As can be seen, nuclear stopping dominates at lower ion energies while electronic stopping takes over at higher ion energies. Typically, the maximum of nuclear stopping occurs at energies of the order of ~ 1 keV.

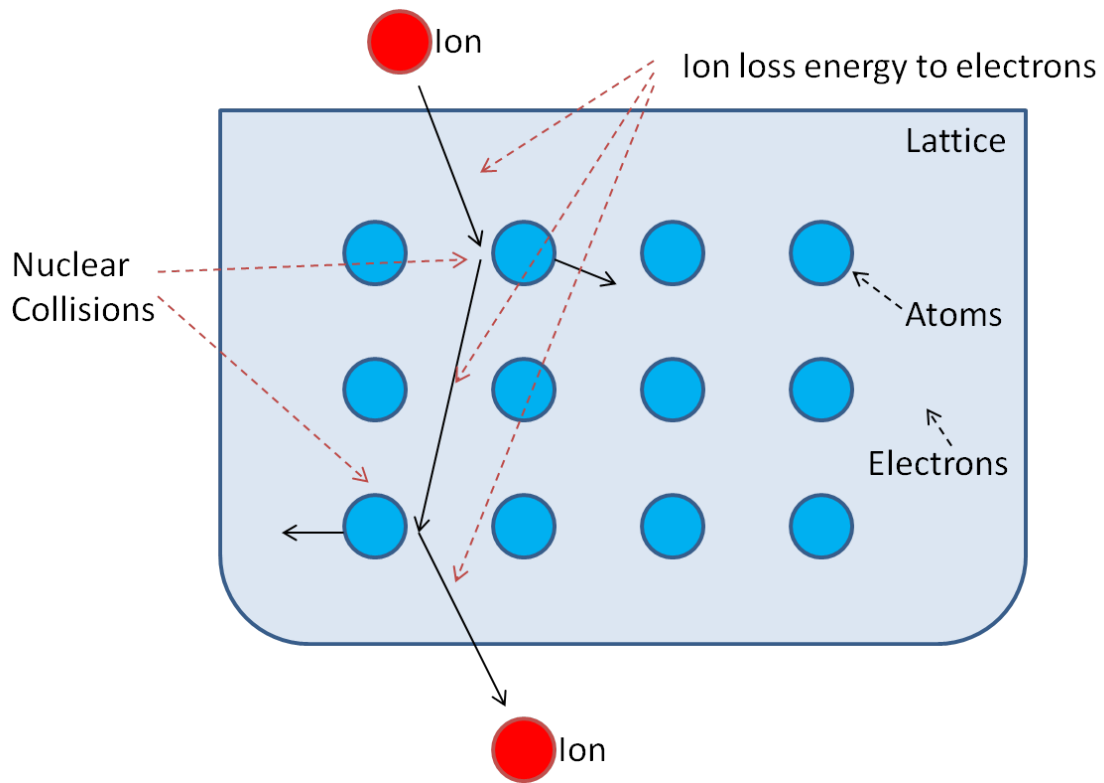


Figure 3.2: A sketch of ion-solid interaction

Nuclear energy loss vs. electron energy loss

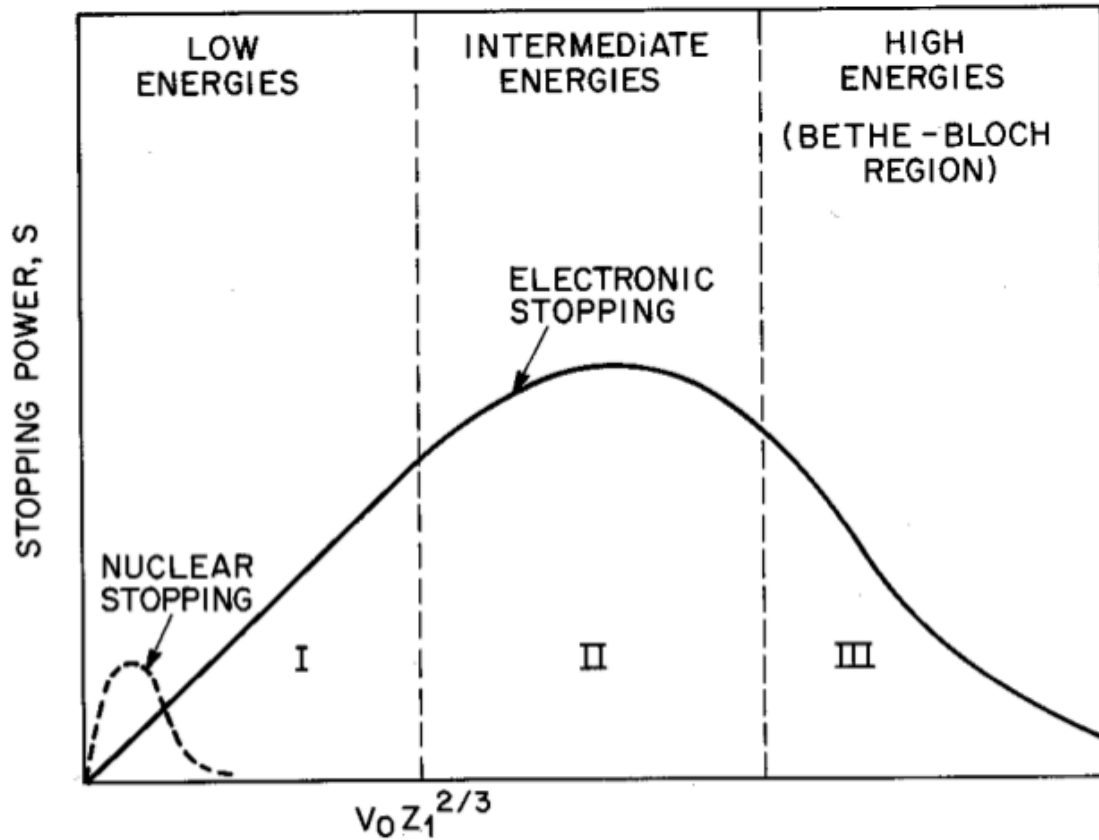


Figure 3.3: The nuclear stopping power and electronic stopping power as a function of ion velocity. V_0 is the Bohr velocity and Z_1 is the atomic number of the ion [36]

Due to the simplified model of MD on electrons, it is not appropriate to use MD simulation for electronic stopping. However, in the case that the energy of primary knock-on atom (PKA) is of the order of keV, MD simulation is a good choice for nuclear collision simulation and thus reproduces the process of nuclear stopping. And at such energy ranges of PKAs, the contribution of electrons can be reasonably neglected.

In MD simulations, the most common method to simulate ion-solid interaction is to introduce damage cascades. Initially, one or more atoms will be assigned with specific

velocities to have kinetic energies larger than their thermal energies. These atoms serve as PKAs. At the beginning, PKAs can be either inside the system or outside and bombarding into the system, depending on the physical processes to be simulated. As PKAs start interacting with other atoms in the system, they transfer energy to other atoms, especially through interatomic collisions. If the kinetic energy of an atom in the system, after receiving energies from other atoms, is larger than the threshold displacement energy of that material, the permanent displacement occurs and defects are produced. The set of these energetic collisions is called the damage cascade.

Typically, the process of a damage cascade can be divided into four phases: the ballistic phase, the thermal spike, the cooling down and the relaxation phase. Figure 3.4 illustrates the evolution of a damage cascade in a ZrC matrix initiated by a PKA of 50 keV [37]. Snapshots taken at 0.05ps and 0.16ps correspond to the ballistic phase, during which numerous ballistic collisions occur and the energies of initial ion/recoil and its primary and lower-order recoils are far above the threshold displacement energy. Some of the recoils travel long enough in the system to create sub-cascade branches, and most of the point defects are created during this phase [37]. The snapshot at 1.4ps represents the thermal spike phase. This phase begins when the kinetic energy of atoms are below the threshold displacement energy but are still high enough to raise local temperature and create heat waves [37]. Theoretically, defects created in this phase will be annihilated during the cooling down and relaxation. Then the system will be cooled down before the relaxation phase takes place. As shown in the snapshot at 12ps of Fig.

3.4, interstitials and vacancies recombination as well as migrations of defects leading to clusters occurs during the relaxation phase.

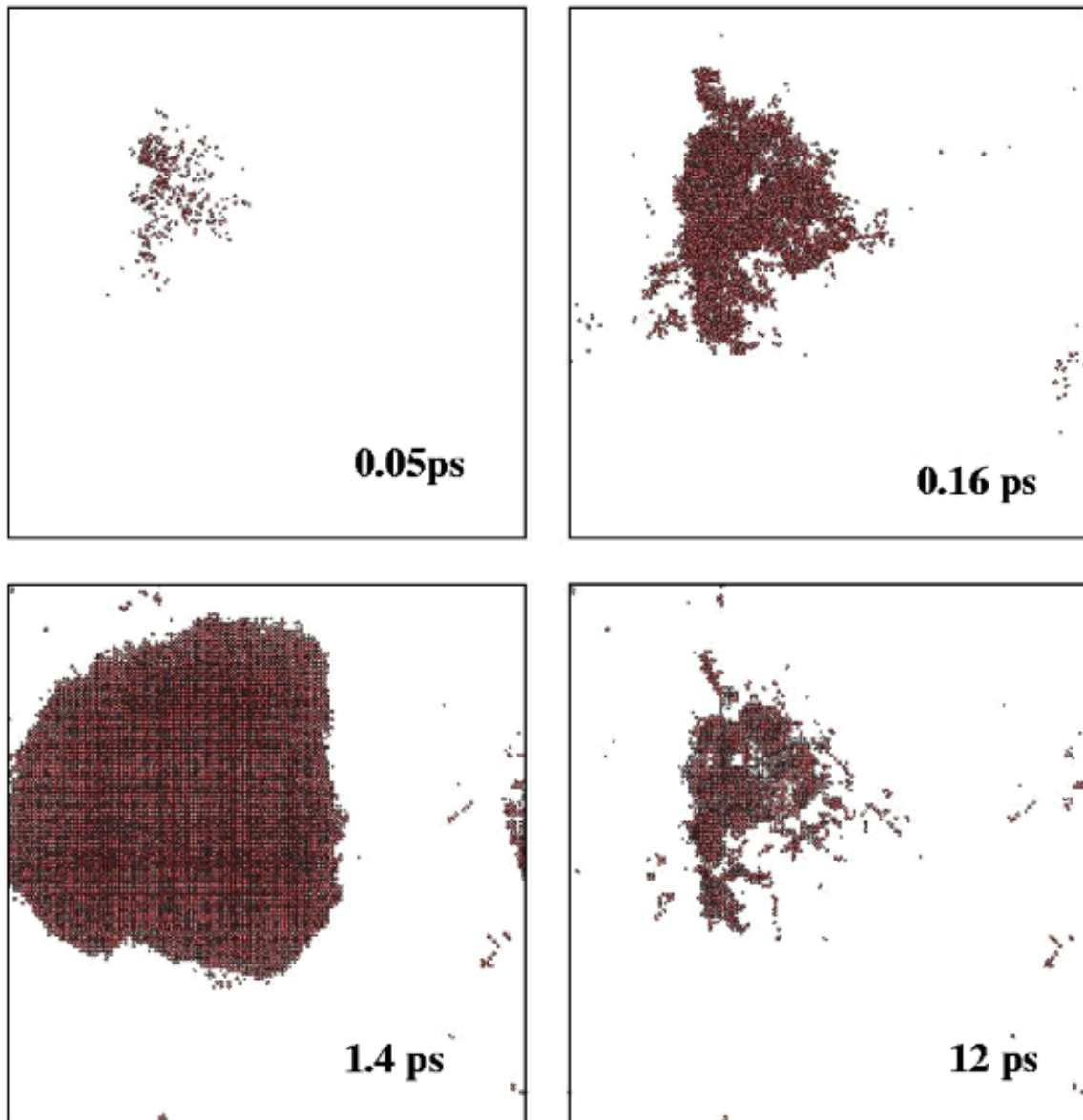


Figure 3.4: Snapshots of a damage cascade in a ZrC matrix initialed by a PKA with initial energy of 50 keV [37]

A common method to analyze defects in MD simulations of damage cascades is to compare the position of atoms in each timesteps with their original positions in the lattice. A threshold value of displacement distance above which an atom is considered as off the lattice site should be determined before carrying out the analysis. If the threshold is too big, then the analysis will be insensitive to displacement events and some defects and microstructures may be ignored; on the other hand, too small threshold will consider thermal vibration as displacement by mistake. This method is employed in our research for defects analyze.

3.3 MD simulations for thermal conductivities

As discussed earlier, MD provides a good simulator for phonon based heat transfer. So it is very promising to use MD simulations for the studies of thermal conductivities. In LAMMPS, there are two ways to carry out the calculation: the Müller-Plathe method [38] and the Green-Kubo method [39]. Despite that we are using Müller-Plathe method in our research, we present both methods here and discuss their pros and cons as well as their different applications.

The Müller-Plathe method is based on the non-equilibrium molecular dynamics method (NEMD). To understand NEMD, we need to start with the definitions of the thermal conductivity, thermal conductance and thermal resistance. The thermal conductivity describes the ability of a material to conduct heat. Better heat conductors have higher thermal conductivities. The thermal conductivity is defined as the heat flux passing through the material over the temperature gradient of the material, when a stable

temperature difference is applied to the system and the system reaches equilibrium. Very similar to thermal conductivities, the thermal conductance is the ratio of heat flux to temperature difference rather than temperature gradient. And a thermal resistance is the reverse of a thermal conductance. Recalling the definition of the Kapitza resistance in section 2.1, we notice that the Kapitza resistance is actually the thermal resistance of an interface/GB. Now it can be seen that all these concepts are about heat flux and temperature difference or temperature gradient. In NEMD, a temperature difference is applied to the two ends of the system, so that a heat flux is formed. As the heat flux gets stabilized during the simulation, both the temperature information and the heat flux can be recorded to calculate the thermal conductivity, thermal conductance or thermal resistance. The Müller-Plathe method is known as a reversed NEMD, in which a heat flux is applied by swapping the most energetic (hottest) atom from one end of the sample with the least energetic (coldest) atom from the other end periodically. Eventually a stabilized temperature profile will form in the system with the heat flux balancing the atom. And the heat flux is stabilized as well. The Müller-Plathe method generates a heat flux to create temperature difference, rather than using temperature difference to generate the heat flux. That is why this method is always referred as a reversed NEMD.

The Green-Kubo method is more complicated. It is based on the fluctuation-dissipation theorem, which is a statistical physics method to predict the behavior of a non-equilibrium system by building a quantitative relation between the fluctuations in the thermal equilibrium system and the response of the system to perturbations [40]. The core calculation of this method is the heat current autocorrelation function, details of

which can be found in Ref. 39. And the thermal conductivity is proportional to the integral of the heat current autocorrelation function over time.

As can be seen, the two methods are fundamentally different from each other. Thus they are applied in different types of studies. The Müller-Plathe method is more direct and comparable to experiments. It is usually applied into more complicated, heterogeneous systems, like systems containing GBs, defects, voids, precipitates, etc. There is always a requirement of the size of a system for the Müller-Plathe method: the totally number of atoms in the system should be large enough to overcome the thermal noise and get reasonable statistic values; the size of the pools at the ends of the system from which atoms are taken and swapped should be big enough to avoid perturbation; more important, the dimension along the heat flux direction should be much larger than the mean phonon free path in that material under the simulation conditions, otherwise unwanted phonon scattering at the two ends of the system will seriously influence the result. To get rid of the size effect especially in the dimension along the heat flux, multiple simulations with only difference in the dimension size L should be carried out. Theoretically, the simulated thermal conductivity k should be proportional to the size L , due to size effect. Hence, by plotting $1/k$ as a function of $1/L$ and extrapolating their correlation to $1/L=0$, which represents the case of unlimited dimension along heat flux, the thermal conductivity without size effect can be found. Figure 3.5 provides an example of the size effect a calculation of the bulk UO_2 thermal conductivity and the $1/k \sim 1/L$ correlation of it [33].

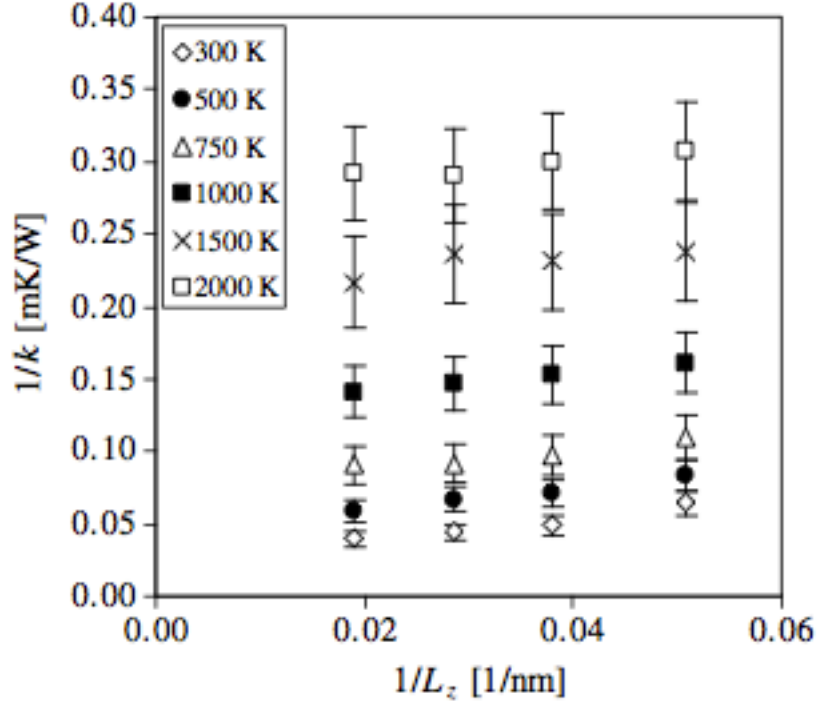


Figure 3.5: Calculations of thermal conductivities in UO_2 system by the Müller-Plathe method for different temperatures and different system sizes [33]

Compared to the Müller-Plathe method, the Green-Kubo method does not require a very large system: size-independent thermal conductivity can usually be obtained using fewer than 10,000 atoms [41]. However, in order to accurately predict the converged value of the heat current autocorrelation function integral, there is a requirement for the total simulation time, which have to be many times greater than the largest phonon relaxation times [41]. That means, the higher the thermal conductivity of a material, the more time consuming the simulation will be. Besides, the Green-Kubo method has a presumption of the system being homogeneous, which makes it an inappropriate choice for systems containing localized phonon scattering centers [42].

3.4 Overview of classical interatomic potentials of UO_2 systems

Many interatomic potentials of UO_2 systems have been developed for the MD simulation. So before carrying out a simulation study, it is very necessary to review these potentials carefully and choose the most appropriate one. We looked through 10 potentials, i.e., Walker-81 [43], Busker-02 [44], Nekrasov-8 [45], Goel-08 [46], Morelon-03 [47], Yamada-00 [48], Basak-03 [49], Arima-05 [50], MOX-07 [51] and Yakub-09 [52, 53].

Two different models have been developed to describe the electrons: the shell-core model and the rigid ion model. The shell-core model raised by Dick and Overhauser takes polarization effects into account by bounding the massless charged shell of the ion to the massive core by spring [54]. Busker-02 is one example of this category. The rigid ion model simplified the ions as massive point charges. Although the shell-core model is more close to the physical fact, most of classical potentials employed in MD simulations take the second model because it is less computational time consuming [55].

One significant difference among these potentials is their treatments to ionicity. We know in stoichiometric UO_2 system, the charge numbers of uranium and oxygen should be +4 and -2 respectively. However as stated in Pauling's empirical formula [56], the electronegativities of elements lead to the effective charge numbers to be less. For the potentials of UO_2 we are discussing now, most of them follow a partial ionicity model although their charge numbers are different. The benefit of partial ionicity is that they can reproduce more accurate properties of defects; and in most cases, the ionicity is determined by fitting to defect energies and the lattice parameters [55]. Because we are

going to simulate damage cascades, we prefer to take the advantage of more accurate defects properties by choosing a partial ionicity model.

On the other hand, we desire a potential with solid performance on thermal properties for the study of the Kapitza resistance of GBs. Potashnikov, et.al have carried out a systemic study on most popular UO_2 potentials and compared their thermal properties [57]. Table 3.1 lists the their calculation results of melting temperatures from different models in various size systems. Noticing that the experimental value of UO_2 melting point is 3140K [58], we can see that all the models predict a higher melting point than experiment, and among them, Yakub-09 predicts a relatively closer value. In addition, as shown in Fig. 3.6 to Fig. 3.8 [57], we can see that the thermal properties of the linear expansion coefficient, isochoric heat capacity and isobaric heat capacity predicted by different models are quite coherent to each other at lower temperatures. But at higher temperatures, i.e. above 1500K, we find that Yakub-09 predicts closer values to IAEA recommendation values. Based on the study by Potashnikov, et.al, we believe that Yakub-09 describes the thermal properties of UO_2 with reasonable accuracy and in a wide temperature range.

Table 3.1: Size dependent melting temperatures of UO_2 predicted by different models [57]

Potentials	Melting temperature (K)			
	N=324	N=768	N=1500	N=12000
Walker-81	4900	4990	4980	5000
Busker-02	6950	7110	7100	7100
Nekrasov-08	4950	5050	5030	5040
Morelon-03	4270	4260	4270	4260
Yamada-00	4960	5000	5010	5000
Basak-03	4170	4200	4200	4200
Arima-05	4520	4550	4550	4550
Goel-08	3840	3830	3840	3840
Yakub-09	3720	3760	3750	3750
MOX-07	4000	3990	4010	4000

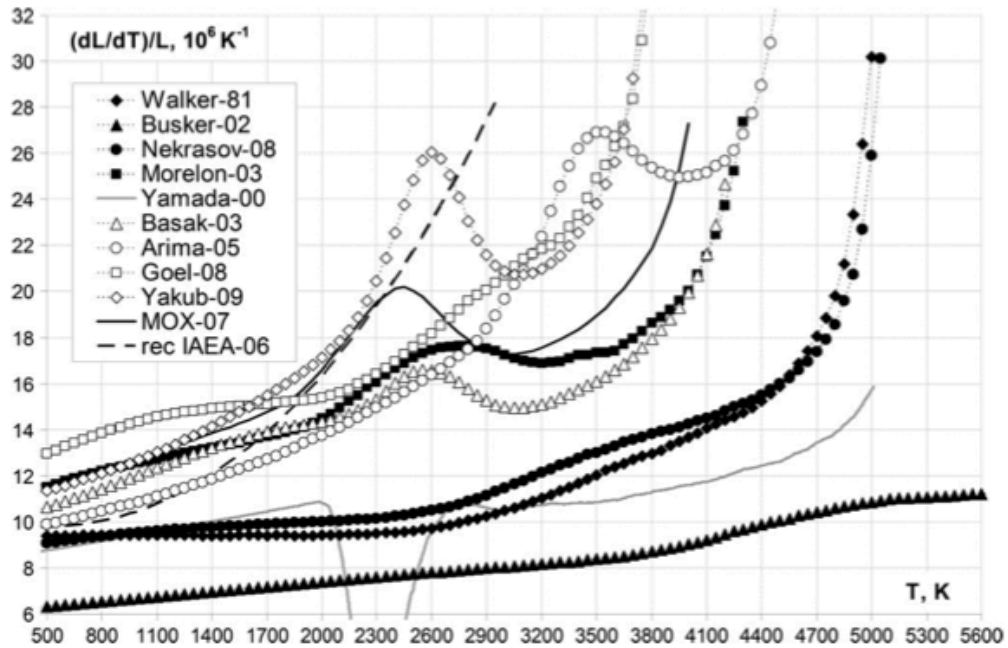


Figure 3.6: Temperature dependent linear thermal expansion coefficients predicted by various models for UO_2 [57]

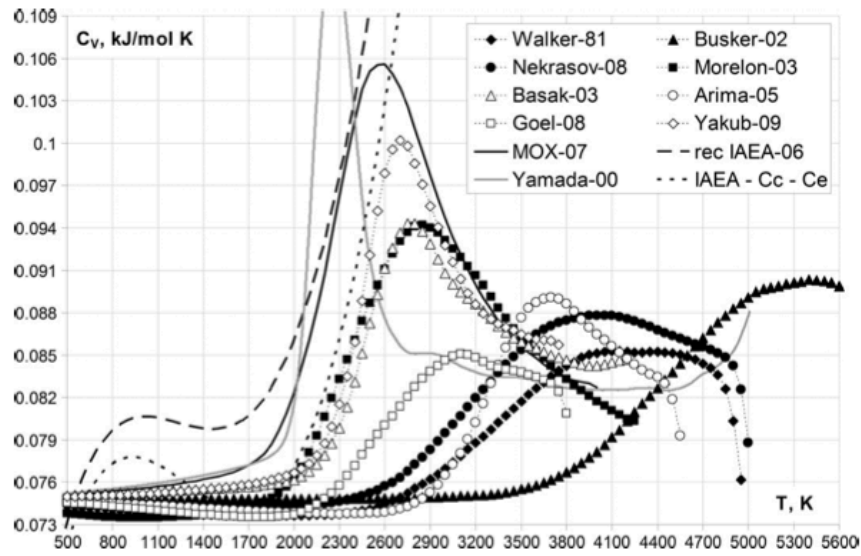


Figure 3.7: Temperature dependent isochoric heat capacities predicted by various models for UO_2 [57]

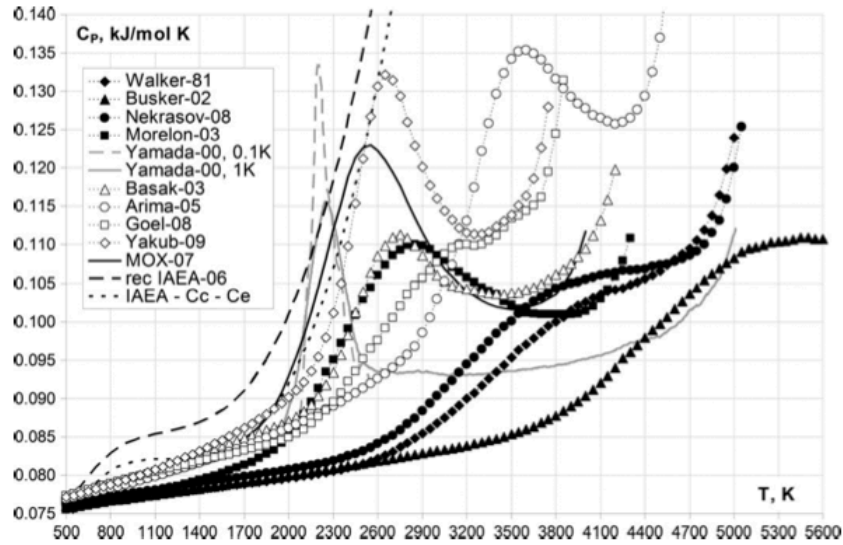


Figure 3.8: Temperature dependent isobaric heat capacities predicted by various models for UO_2 [57]

While the details of Yakub-09 potential can be found in Ref. 52 and 53, we point out here a few points worth noticing. The pair interionic potential consists of a short-range part and a Coulombic part. The short-range part consists of a dispersion term to represent van der Waals attraction, a short-range overlap repulsion term for closed electronic shells, and a covalent bonding term. The law of Coulombic describes the Coulombic part with the ionicity to be 0.5552, meaning that U^{4+} carries 2.2208e charges and O^{2-} carries -1.1104e charges. The defects formation energy calculated by this potential reasonably agree with experimental and ab-initio data [52]. Besides, this model also includes U^{5+} and helium atoms, providing the ability to study non-stoichiometric systems and systems with the fission gas.

4. DAMAGE CASCADES IN BICRYSTAL UO_2 SYSTEM

We carried out a serial of damage cascade simulations in UO_2 systems with different configurations. Our purpose is to understand the interaction of GBs and defects as well as the structural changes of GBs during the damage cascade. We chose $\Sigma 5$ GB because it has been frequently used in previous studies and observed in experiments[27, 28]. We introduced our damage cascades by assigning initial energies to selected uranium atoms as the PKAs. To understand the interaction between the GB and damage cascades, we used two different energies for PKAs to simulate two different situations: one is to ensure that damage cascade penetrates the GB through ballistic collisions, which is refereed as the direct interaction later; the other one with a smaller PKA energy is used to simulate the case when no ballistic collisions occur on the region of the GB and the cascade mainly interact with the GB through thermal interactions, which is referred as the indirect interaction. For the purpose of comparisons, we also introduced the same damage cascades into monocrystal systems. Before we carried out our damage cascade simulations, we attached the Ziegler-Biersack-Littmark (ZBL) potential [59] for short-range interatomic interaction to Yakub-09 potential. Details are presented in section 4.1; and then we conducted the direct and indirect interaction simulations, as described above, in section 4.2 and 4.3 respectively. Finally in section 4.4, we discuss our observations and conclusions.

4.1 The Ziegler-Biesack-Littmark potential

During damage cascades, some atoms carry so high kinetic energies that there is a good chance for two atoms to come very close to each other, i.e., less than 1 angstrom. At distance comparable to the Bohr radius (0.539177 angstroms), the potential energy is much more complex and it is not appropriate to describe the interatomic potential by models whose parameters are fitted by material properties in equilibrium systems. Overall, polarization effects, shell structures, electrons excited or ejected during the collision, etc. can all affect the short-range interatomic interaction. In the case of high collisional energies, we can assume that nuclei approach so close that we can neglect attractive forces and consider repulsive interactions purely [59]. And ZBL potential serving as a screening electrostatic potential of nucleon-nucleon interaction, applies to this situation very well.

To connect ZBL potential to Yakub-09 potential, we employ a fifth degree polynomial as a connection function to ensure continuous transition points of the forces and their first derivatives. Figure 4.1 shows the connection of the ZBL potential to Yakub-09 potential in the case of the potential energy for uranium-uranium interaction as an instance. We can see that there is a significant difference between the ZBL potential and Yakub-09 potential in short range. So it is very necessary to apply the ZBL potential for more accurate description of the damage cascade process. The transition region, that is the ranges of connection functions, varies for interactions with different ion-pairs, as listed in Table 4.1. The region of r less than r_1 is described by ZBL potential;

the region of r larger than r_2 is described by Yakub-09; and the region of r in between r_1 and r_2 is taken over by the connection function.

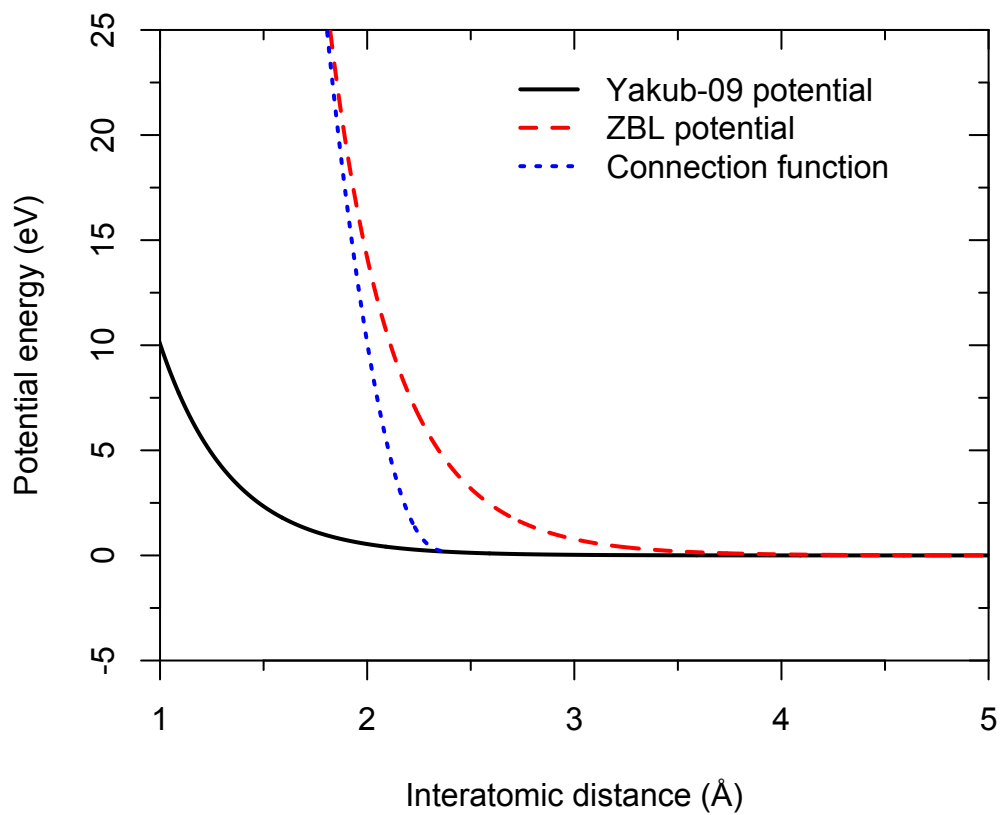


Figure 4.1: The connection of Yacub-09 potential and ZBL potential

Table 4.1: Transition regions for different ion-pairs.

Ion-pair	$\text{U}^{4+}\text{-U}^{4+}$	$\text{O}^{2-}\text{-O}^{2-}$	$\text{U}^{4+}\text{-O}^{2-}$
r_1 (Å)	1.5	0.8	0.5
r_2 (Å)	2.4	1.8	1.0

4.2 The direct interaction of damage cascades and GBs

As mentioned at the beginning of section 4, we simulated with different PKA energies to study the direct and indirect interactions. We used a 3keV PKA to create a damage cascade that penetrates the GB during ballistic phase, i.e., the direct interaction; and we used 1.5keV PKA to simulate the case when the GB is free from collisions, i.e., the indirect interaction. In this section, we report the direct interaction case as well as a comparable simulation of a damage cascade in monocrystal system initiated by a 3keV PKA.

We constructed the $\Sigma 5$ (012)[100] GB with the help of GBstudio [60]. The bicrystal system of 5.5nm x 7.4nm x 9.9nm in size, with the GB in the x-y plane at z=5.0 nm was annealed at 2000K for 30ps for structural relaxation then brought to equilibrium at 1000K before damage cascade was induced. This relaxation strategy has been frequently used in previous studies [25, 28] and will be used in our later simulations in section 5. We conducted our damage cascade simulation at 1000K to accelerate the process. One uranium atom at the distance of 1.6nm from the GB was assigned with a kinetic energy of 3 keV, as PKA. Initial velocity of PKA was towards the GB. The system was under constant volume and constant energy for 1.3 ps before the thermal spike phase finishes, and then annealed at 1000K under constant volume for a successive period of 65 ps. Figure 4.2 shows snapshots of the damage cascade. Figure 4.2 (a) shows the ballistic phase during which collisions occur and recoils are created; Figure 4.2 (b) shows how the thermal spike creates more defects, most of which are annihilated during

the cooling down phase as shown in Fig. 4.2 (c); And eventually after relaxation, as shown in Fig. 4.2(d), more defects are annihilated and the system becomes stabilized.

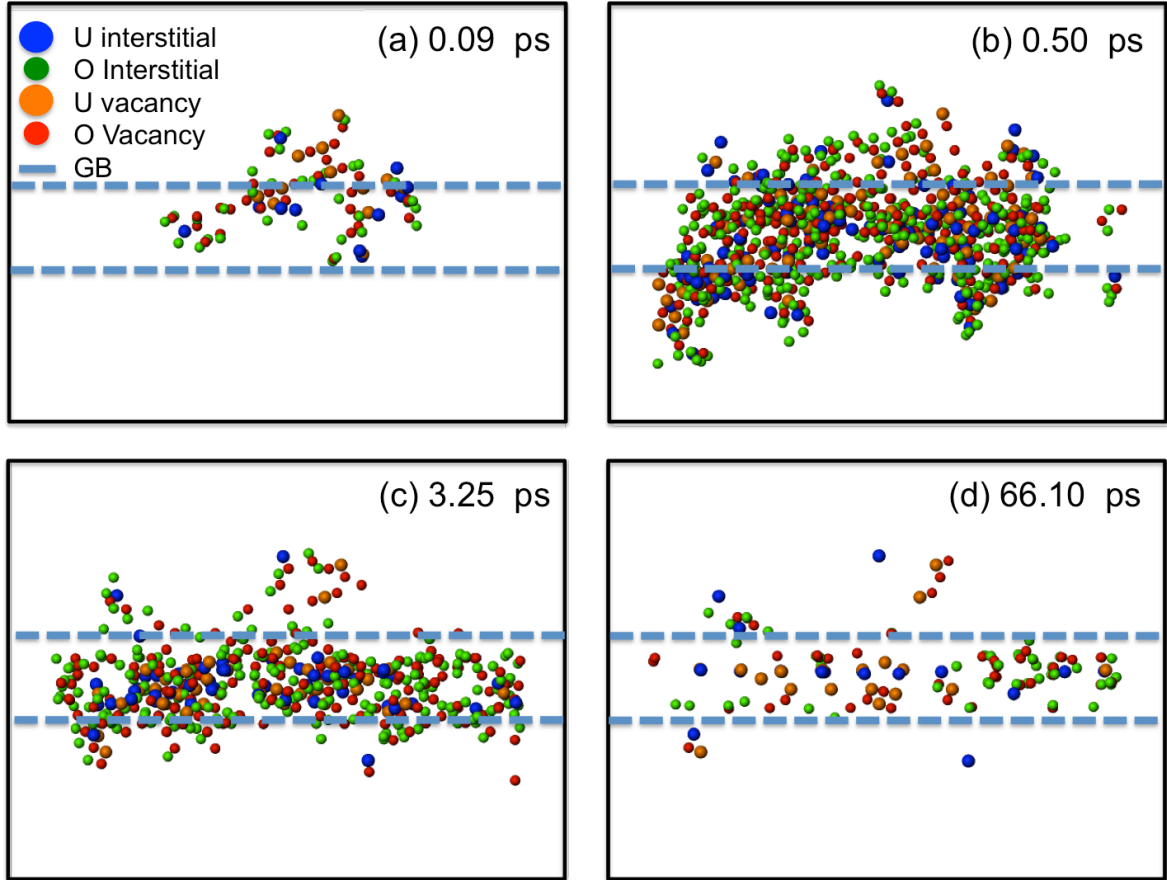


Figure 4.2: Snapshots of a damage cascade initiated by the a 3 keV PKA in the $\Sigma 5$ (012)[100] system; the GB is between the two dashed lines

Figure 4.3 provides a more quantitative look into the damage cascades evolution as well as the comparison between the 3keV damage cascade in the bicrystal system (colorful lines) and the damage cascade of same energy in the monocrystal system (black lines). First it is very obvious that during the ballistic and thermal spike phases, the total defects created in the bicrystal system are more than it in the monocrystal system. This

agrees with the observations of Van Bruzel and provides evidence that the GB serves as a point defects rich region where displacements are welcome to take place. In other words, the GB captures some recoiled atoms and dissipates their energies, which has been reported by Van Bruzel [27, 28]. As a result, some atoms in the GB are knocked out into the grain region and become interstitials. And that is why there is more interstitials than vacancies in the grains for both uranium and oxygen at the thermal spike peak as shown in the embedded profile in Fig. 4.3. Moreover, we notice that the number of oxygen atoms knocked out from the GB is about 5 times of the number of knocked out uranium atoms, due to the lower displacement threshold energy of oxygen atoms than uranium atoms. This suggests that the grain boundary lose its electrical neutrality during the ballistic phase; as a result, the Coulombic effect between the GB and the defects in the grains is enhanced. Since the Coulombic interaction has a long range, we believe it plays a significant role in the evolution of defects. For the sake of oxygen defects in grains, it evolves from interstitial rich before 2 ps to vacancy rich after 6 ps. Two mechanisms could contribute to the demolition of interstitials: one is the local interstitial-vacancy annihilation during cooling down, which occurs in grains as well as in the GB; the other is through interstitials migration towards the GB. From Fig 4.4(a-c), it can be seen that some oxygen atoms in the vicinity of the GB formed some “ring pattern” structures similar to the structure of the GB itself, as shown in the dashed box in Fig. 4.4(c). And after annealed in 65ps, as shown by Fig. 4.4(d), most of these trapped atoms are recombined with vacancies during relaxation. And for oxygen interstitials that

could not get absorbed, the GB loads them onto its surface and adhere them, for example the interstitial cluster boxed by dashed line in Fig. 4.4(e-g).

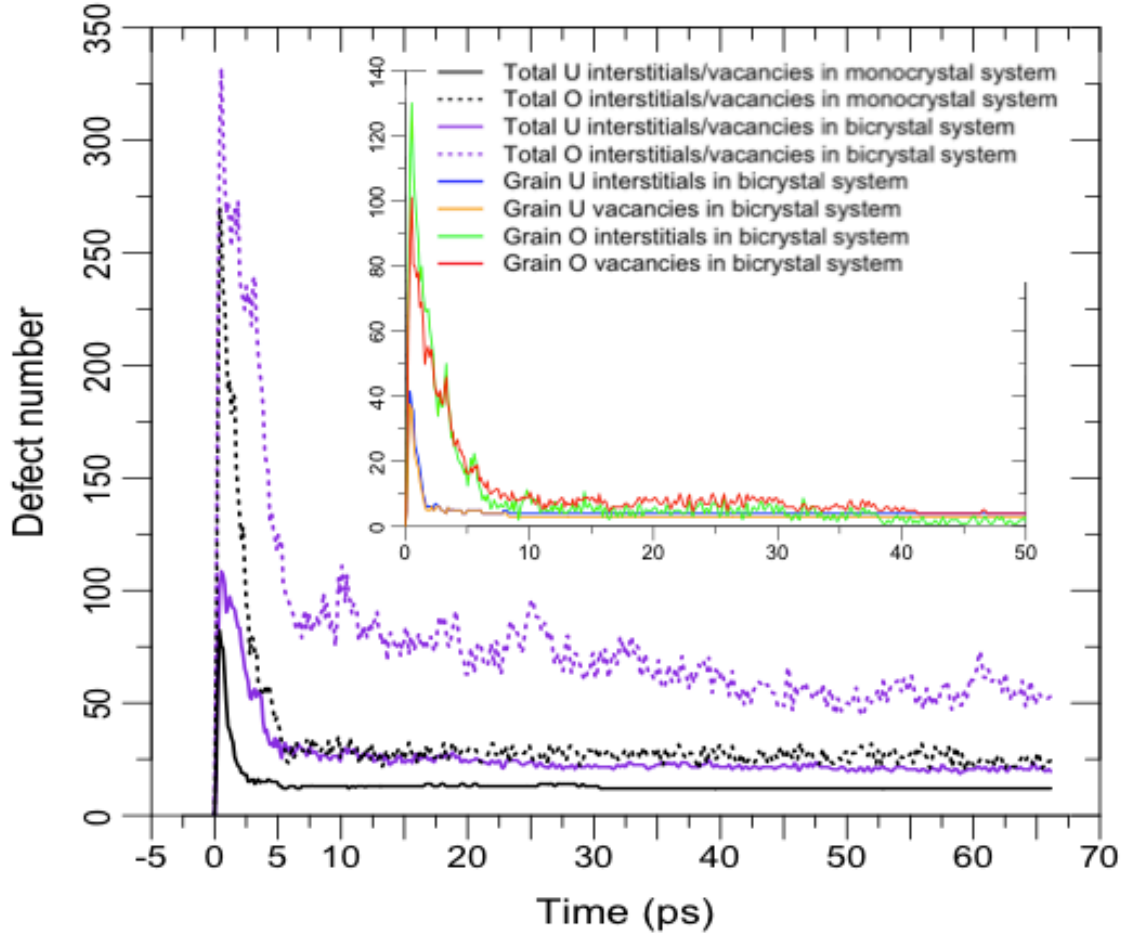


Figure 4.3: Numerical analysis of defects in the 3 keV damage cascade in bicrystal and monocrystal systems. The embedded figure shows the profile of different types of defects in grains of the bicrystal system

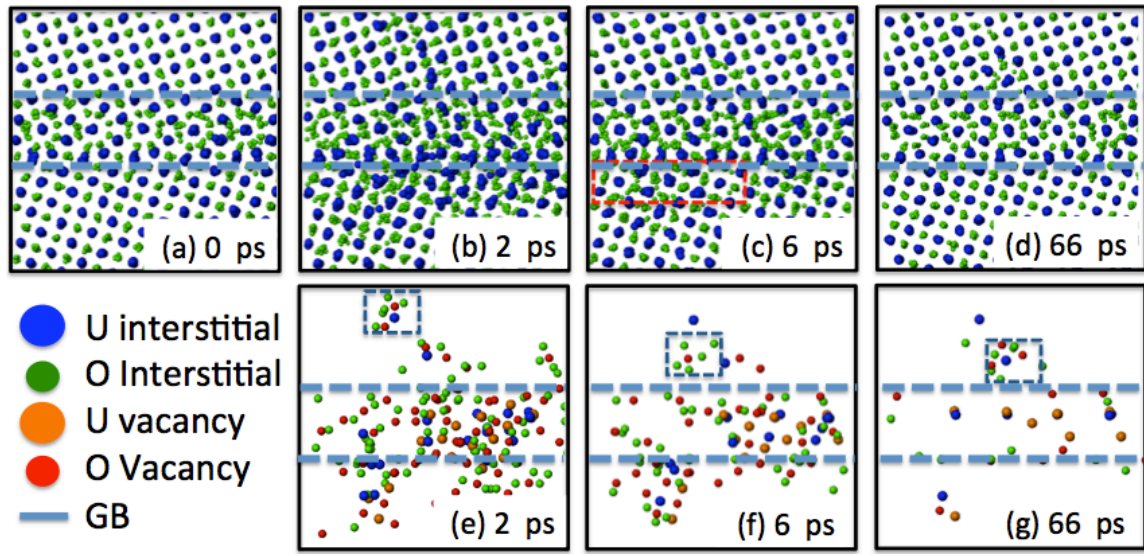


Figure 4.4: $\Sigma 5$ GB structure changes during the damage cascade. (a) is the structure before damage cascade; (b-g) are the evolution of the GB; (e-g) are the defects analysis corresponding to (b-d)

Figure 4.5 shows the snapshots of the damage cascade initiated by the 3keV PKA in a monocrystal system. Compare Fig. 4.5(a), which is the thermal spike at 0.5ps, to Fig. 4.2(b), the shape of the cascade in the monocrystal system is more sphere-like, showing agreement to Van Brutzel's observation of weak correlation between the initial orientation of the PKA and the cascade morphology in UO_2 matrix [61]. On the other hand, the shape of the cascade in the bicrystal system is elongated along the GB, showing more evidence that the energy of the cascade is dissipated by the GB. Figure 4.5(b) is taken at 66.1ps when the system is pretty much relaxed. The number of defects in the monocrystal system is larger than it in the grains of the bicrystal system. And most of the defects are in form of clusters. Due to the lower mobility of uranium defects and the absorbing forces they applying to oxygen defects of the same type, we suggest that the uranium defects serve as clustering cores during cluster formation in the UO_2 matrix.

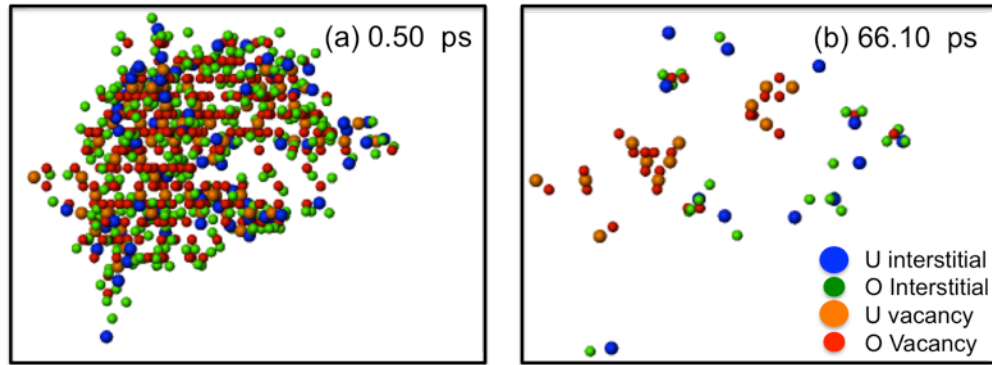


Figure 4.5: Snapshots of the damage cascade initiated by the 3 keV PKA in a UO_2 monocrystal system

4.3 The indirect interaction of damage cascades and GBs

To study the case when no ballistic collision occurs on the GB, we conducted the damage cascade simulations with the energy of PKAs being 1.5 keV in both bicrystal and monocrystal systems. For the bicrystal system, the damage cascade does not have overlap with the GBs as shown in Fig. 4.6(b), and we did not observe any atoms captured by the GBs or any atoms in the GBs knocked out. However, plenty of defects appeared in the GBs during our simulation, which can be seen in Fig. 4.6, probably due to perturbation brought by the cascade through thermal interactions. As shown in Fig. 4.6(a), these defects in the GBs begin to show up at the very early stage of the damage cascade. Although there is no direct interaction between the GBs and the damage cascade as in the case of 3 keV damage cascade, we observed the interaction between the GBs and the defects in the grain caused by damage cascade, as shown in the red circle in Fig. 4.6(c). After relaxation, clusters formed in the grain as shown in Fig.

4.6(d). Although initiated by lower PKA energy, there are more defects remain after relaxation in the case of indirect interaction than it in the case of direct interaction, hinting that the direct interaction enhanced the ability of GBs to trap defects.

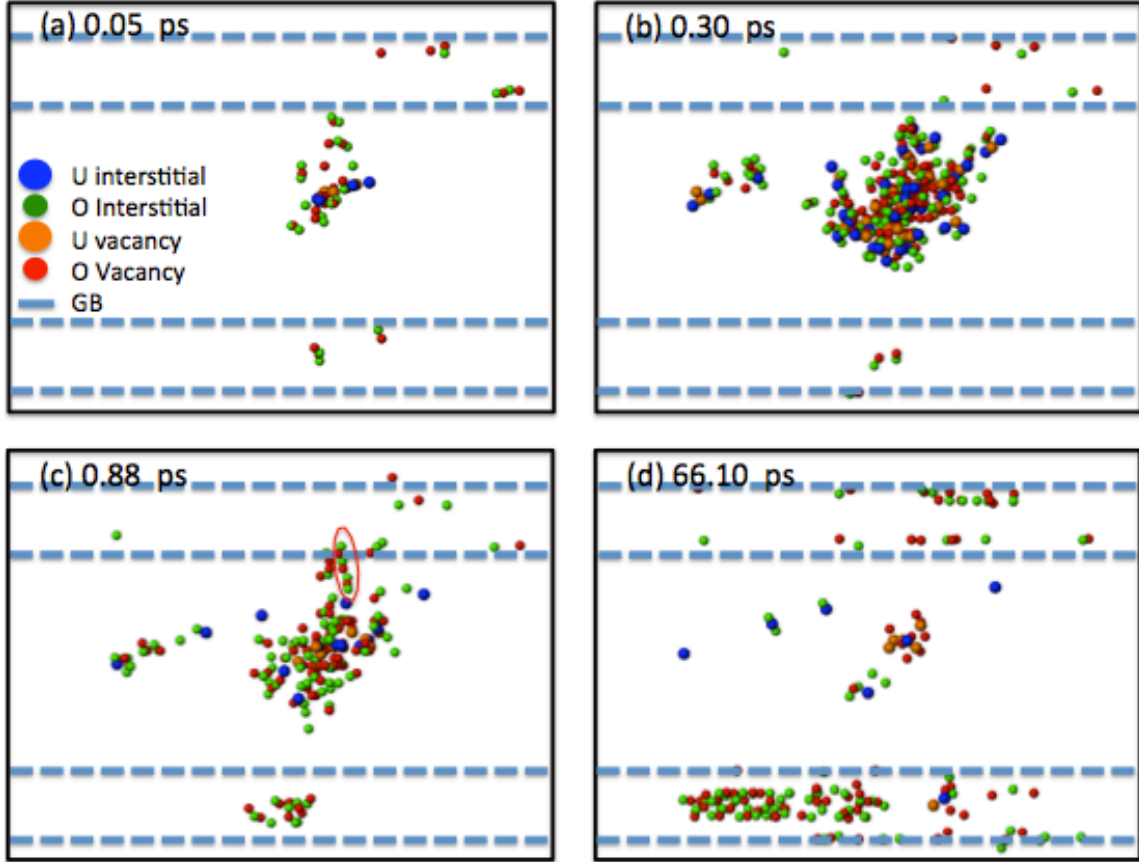


Figure 4.6: Snapshots of the damage cascade initiated by the 1.5 keV PKA in the $\Sigma 5$ (012)[100] system; the GB is between the two dashed lines

We also carried out the simulation of the damage cascade initiated by 1.5 keV PKA in a monocrystal system. The snapshots of the thermal spike and the defects after relaxation are shown in Fig. 4.7(a) and (b) respectively. This damage cascade is not significantly different from the one initiated by 3 keV PKA in the monocrystal system

shown in Fig. 4.5 except that less defects were produced initially and remained after relaxation.

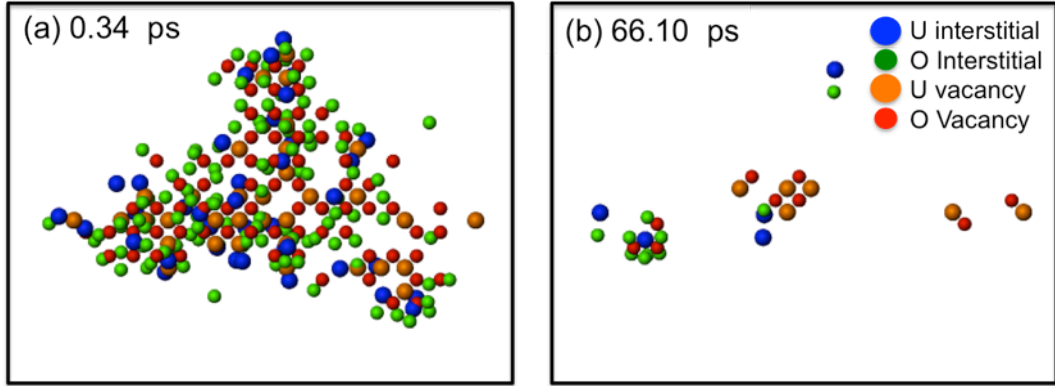


Figure 4.7: Snapshots of the damage cascade initiated by the 1.5 keV PKA in the UO_2 monocrystal system

Figure 4.8 illustrates the comparison between the damage cascades initiated by 1.5 keV PKAs in the bicrystal system and the monocrystal system. We can see that the number of defects generated during the thermal spike in the grains of bicrystal system is slightly lower than it in the monocrystal system. However they become roughly same during and after cooling down and relaxation. So we believe that the GBs in UO_2 do not serve as a sink of defects in this case when there is no direct interaction between them and the damage cascade. The lower number of defects at thermal spike of the bicrystal is due to the fact that some thermal energy is dissipated into GBs, which causes the interstitial-vacancy pairs in GBs as shown in Fig. 4.6. By comparing Fig. 4.8 to Fig. 4.3, we noticed that there is no difference in the numbers of interstitials and vacancies of the same type of element in the grains at the thermal spike for the case of 1.5 KeV damage

cascade. In contrast to our previous case where the GB loses its electrical neutrality by interacting with the 3 KeV damage cascade, the GBs in the indirect interaction case do not capture or lose atoms, and thus remain their electrical neutrality during the damage cascade evolution.

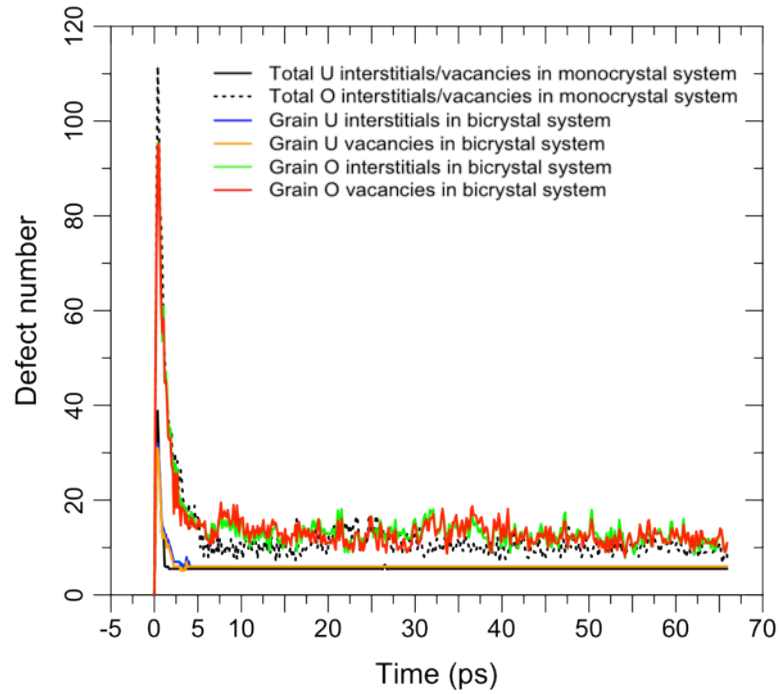


Figure 4.8: Numerical analysis of defects of the damage cascades initiated by the 1.5 keV PKAs in UO_2 bicrystal and monocrystal systems

4.4 Conclusions and comparisons of direct and indirect interactions

In sections of 4.2 and 4.3, we presented the damage cascade simulations in bicrystal UO_2 systems with $\Sigma 5$ GBs in the systems. We employed different PKA energies to conduct direct and indirect GB-damage cascade interactions. By comparing

damage cascade simulations in bicrystal systems to damage cascade simulations in monocrystal systems, we observed the behaviors and roles of GBs during damage cascade. Table 4.2 concisely presents our simulation configurations and our observations from them. We observed that the GB traps defects only in the case of direct interaction between the GB and the damage cascade. The early behaviors of capturing atoms and dissipating energies of the GB due to ballistic collisions actually enable the GB to trap and load defects. Losing and regaining the electrical neutrality of the GB influences the evolution of the GB-damage cascade interactions. We suggest that the Coulombic force serves as a driving force of the GB to capture defects.

Table 4.2: Damage cascade simulations in bicrystal UO_2 systems

Simulation cases	Case 1	Case 2
PKA energies	3 keV	1.5 keV
GB-damage cascade Interactions	Direct: the GB captures atoms and dissipates energies from recoiled atoms in ballistic phase.	Indirect: GBs are perturbed by the damage cascade however do not capture or lose atoms.
Electrical neutrality of GBs	Lose electrical neutrality due to atoms knocked out from the GB.	Remain electrical neutrality.
Defects in grains after relaxation	Less than the defects induced by the same energy PKA in the monocrystal system.	Roughly same to the defects induced by the same energy PKA in the monocrystal system.
Defects loaded onto GBs	Yes, oxygen interstitial clusters loading observed.	No defects loading onto the GB observed.

As a result of the interactions with damage cascades, the GBs undergo structural changes, as illustrated in Fig. 4.2, Fig. 4.4 and Fig. 4.6. We care about the evolution of GBs during the damage cascade. We use the GB energy as a characteristic property of the GB to investigate its evolution during the damage cascade. The GB energy is the

excess free energy, compared to the perfect lattice as the reference, which associated with the state of a GB. It can be calculated by [62]:

$$\gamma = \sum_{i=1}^N (\sum_{j \neq i} \phi(r_{ij}) - \phi_B) / A,$$

where $\phi(r_{ij})$ is the potential energy between atom i and atom j , ϕ_B is the potential energy of the atom in perfect bulk lattice, and A is the area of the GB. We calculated the GB energy changes during the damage cascade, as shown in Fig. 4.9. The red line represents the case of direct interaction between the GB and the damage cascade as discussed in section 4.2; the black line represents the indirect interaction case as discussed in section 4.3. The peak energy for the direct interaction case is much higher and comes earlier than the peak energy for the indirect interaction case. That is because the GB gains more energy through ballistic interaction between atoms in the direct interaction; while for the indirect interaction, the interaction between the GB and the damage cascade is through thermal interaction, and only a small portion of the kinetic energy are transferred to the GB. For the indirect interaction case, the presence of GB has very little influence to the ballistic phase of the damage cascade. After relaxation, the GB energy for the direct interaction case increases due to the defects loaded to the GB; however, the GB energy for the indirect interaction does not change, which agrees with our previous observation that no defects are loaded to the GB. It also suggests that the defects on GBs shown in Fig. 4.6 are due to the perturbation and the method of defects analyses we used. The GBs in the case of indirect interaction actually remain their low-energy structures after the damage cascades.

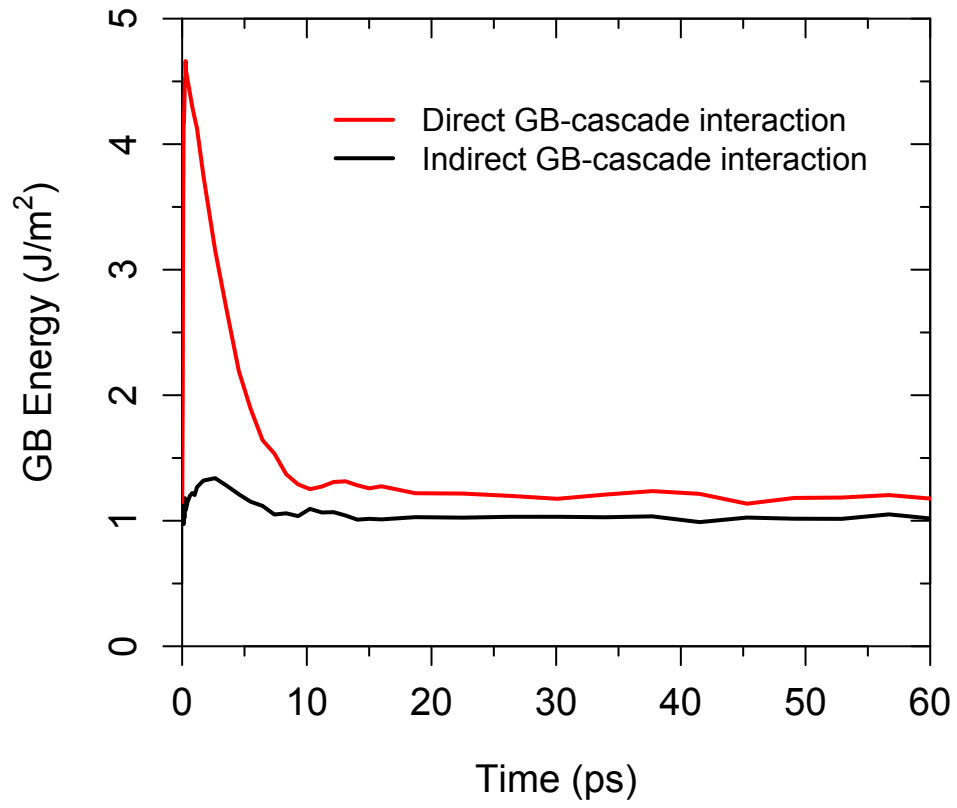


Figure 4.9: The evolution of GB energies during the damage cascade for direct and indirect GB-cascade interactions in UO_2 bycrystal systems

5. THE KAPITZA RESISTANCE OF GRAIN BOUNDARIES

In this section we present our calculations of the Kapitza resistance and the Kapitza lengths of different bicrystal UO_2 systems. We also calculated their corresponding GB energies and managed to find a correlation between the Kapitza resistance and the GB energy. The structure of this section is arranged as follow: in section 5.1, we introduce our simulation configurations and some details on the simulated data processing; in section 5.2 we show our simulation results of Kapitza resistances of different CSL GBs; in section 5.3 we present our work in introducing defects loads to some GBs and how they influence the Kapitza resistance; and finally in section 5.4, we bring out a correlation between the Kapitza resistance of the GB and its corresponding GB energy that works for both cases of different CSL boundaries and different levels of defect loads on GBs.

5.1 Simulation configurations and calculations of the Kapitza resistance

When constructing different CSL boundaries with GB studio [60], we managed to keep the systems roughly similar in size, with the cross-section to be approximately 3nm, by 3nm and the length of the system to be around 20nm. The GB is parallel to the cross-section and settled in the middle of the length of the simulation box. It has been shown in previous studies that the Müller-Plathe method is not sensitive to the area of cross-section of the simulation box [33, 63]. But there is a size effect from the limited length of the simulation box. For comparisons with experimental data, multiple MD simulations need to be run for different system sizes and the size dependence is used to

extrapolate the value corresponding to macroscopic scale, as discussed in section 3.3 for the case of thermal conductivity calculations. For our present study, our key interest is to compare the Kapitza resistance changes instead of the size effect, so we did not carry out the extrapolation calculations, and our length of the simulation boxes is reasonable. The as-constructed boundaries contain atoms occupying high energy sites. Therefore, a structural relaxation step is needed to minimize energy. In the present study, each boundary structure was equilibrated at 2000K for 2.5 ps and then slowly cooled down to 300K. It has been shown that for small angle boundaries, the relaxed structures contain edge dislocations, while for high angle boundaries, relaxation leads to vacancy-contained specific patterns [28]. Depending on interatomic potential used, relaxation mechanism and relaxed structures can be different [25]. Atoms at boundaries have different coordination numbers, leading to enhanced potential energies. As shown in Fig. 5.1, the potential energy peak is not exactly at the interface and energy distribution depends on specific configurations. The width of a GB can be calculated based on the criteria that a boundary atom's potential energy needs to differ from the bulk value by a certain value [28]. Figure 5.1 illustrates the atomic potential energy in reference to the bulk of a $\Sigma 9$ (5 4 2)/(4 5 2) GB system and the GB region determined for the system. We can also see from Fig. 5.1 that the change in uranium atomic potential due to the presence of the GB is more dominating than the change in oxygen atomic potential.

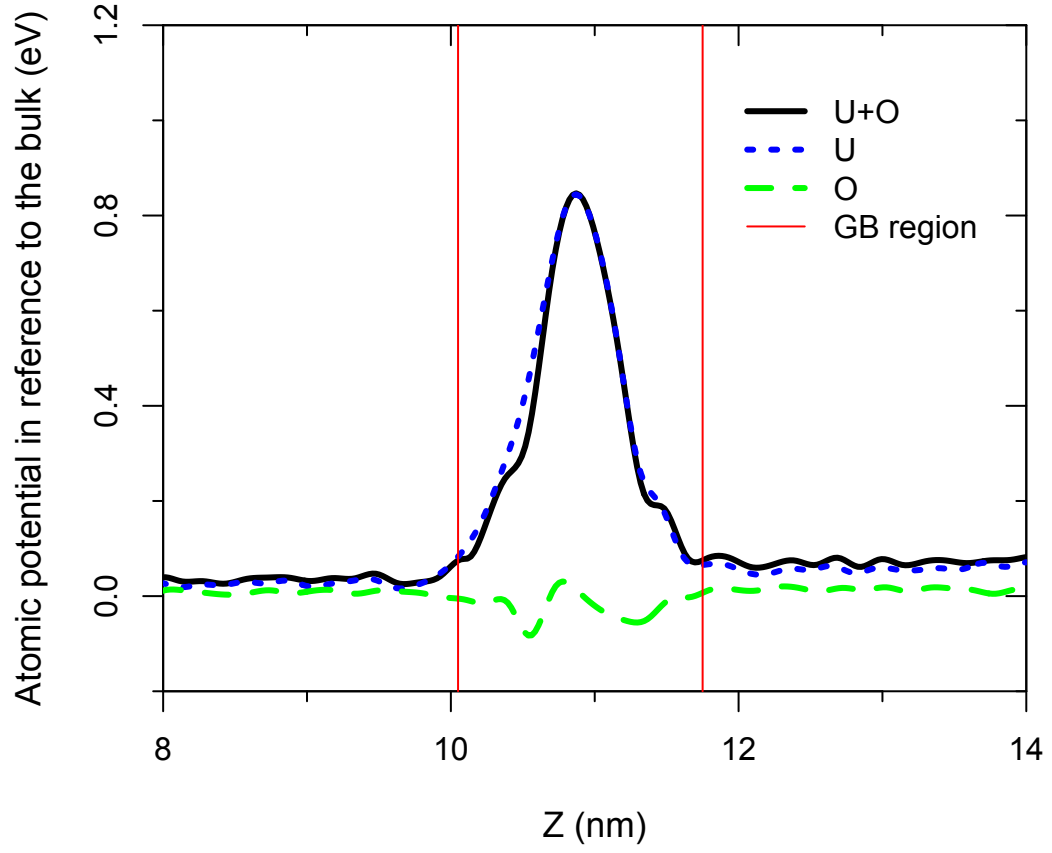


Figure 5.1: The atomic potential energy in reference to the bulk of a $\Sigma 9 (5\ 4\ 2)/(4\ 5\ 2)$ bicrystal system

For the simulation of heat transportation in the system and the calculation of the Kapitza resistance of the GB, we employed the Müller-Plathe method, due to its advances as discussed in section 3.3. To apply that method, as shown in Fig. 5.2, we divided the simulation box into multilayers with two end layers referred as a “hot” end and a “cold” end, respectively. Periodically, the hottest atom in the cold end is identified and the coldest atom in the hot end is identified. These two atoms are paired up and their

velocities are exchanged. This is equivalent to exchange their kinetic energies if two atoms have the same mass. Such kinetic energy exchange induces a heat flux from the hot side to the cold side. Eventually the heat flux will balance the kinetic energy exchange and thus the system reaches equilibrium condition in which both heat flux and temperature at any point are insensitive to simulation times.

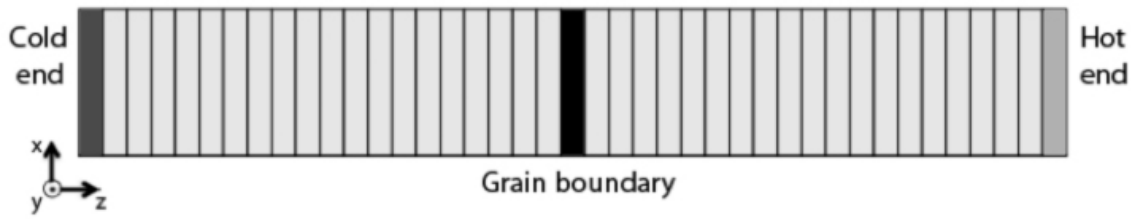


Figure 5.2: The multiple layer structure of the simulation box for the Müller-Plathe method

We carried out simulations of the Müller-Plathe method for 100 ps to make sure that the simulation systems reach equilibrium condition before we have enough data to collect. Fig. 5.3 plots the heat flux changes as a function of times for three systems: a bulk system, a system containing a $\Sigma 5$ (0 1 2)[1 1 0] GB and a system containing a $\Sigma 9$ (5 4 2)/(4 5 2) GB. The heat flux quickly drops in a few ps after the kinetic energy exchange starts and it becomes saturated and statistically smooth at times longer than 40 ps. The times required for data converging are slightly different for different boundary configurations. For consistency all thermal resistance data in the present study were calculated by averaging the values between 55 ps and 100 ps.

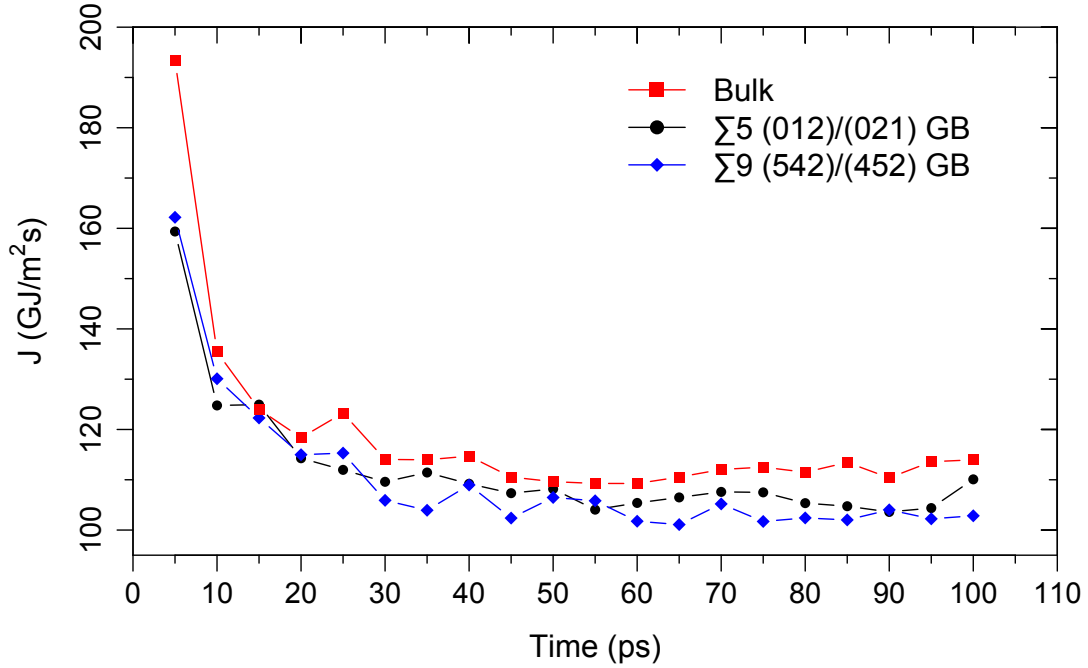


Figure 5.3: The evolution of heat flux during of the Müller-Plathe method simulation. Red points refer to the bulk; black points refer to the $\Sigma 5$ (0 1 2)[1 1 0] GB; and blue points refer to the $\Sigma 9$ (5 4 2)/(4 5 2) GB.

Figure 5.4 shows the temperature profile as a function of distance of the same systems as in Fig. 5.3. It corresponds to the simulation time 55ps, which is late enough to achieve stabilized heat flux. On each side of the grain boundary, temperature gradients with essentially the same slope are established, which is governed by the bulk thermal conductivity. Across the GB in the middle there is a large temperature difference, as a result of phonon scattering from discontinuous boundaries. Substituting ΔT from Fig. 5.4 and J from Fig. 5.3 into $R = \Delta T / J$ obtains corresponding GB thermal resistance. We also calculate the GB energy as described in setion 4.4 and the Kapitza length, as defined in

section 2.1 and Fig. 2.5, by $l_{\kappa} = \kappa \times R$, where κ is the thermal conductivity of bulk material under the same condition.

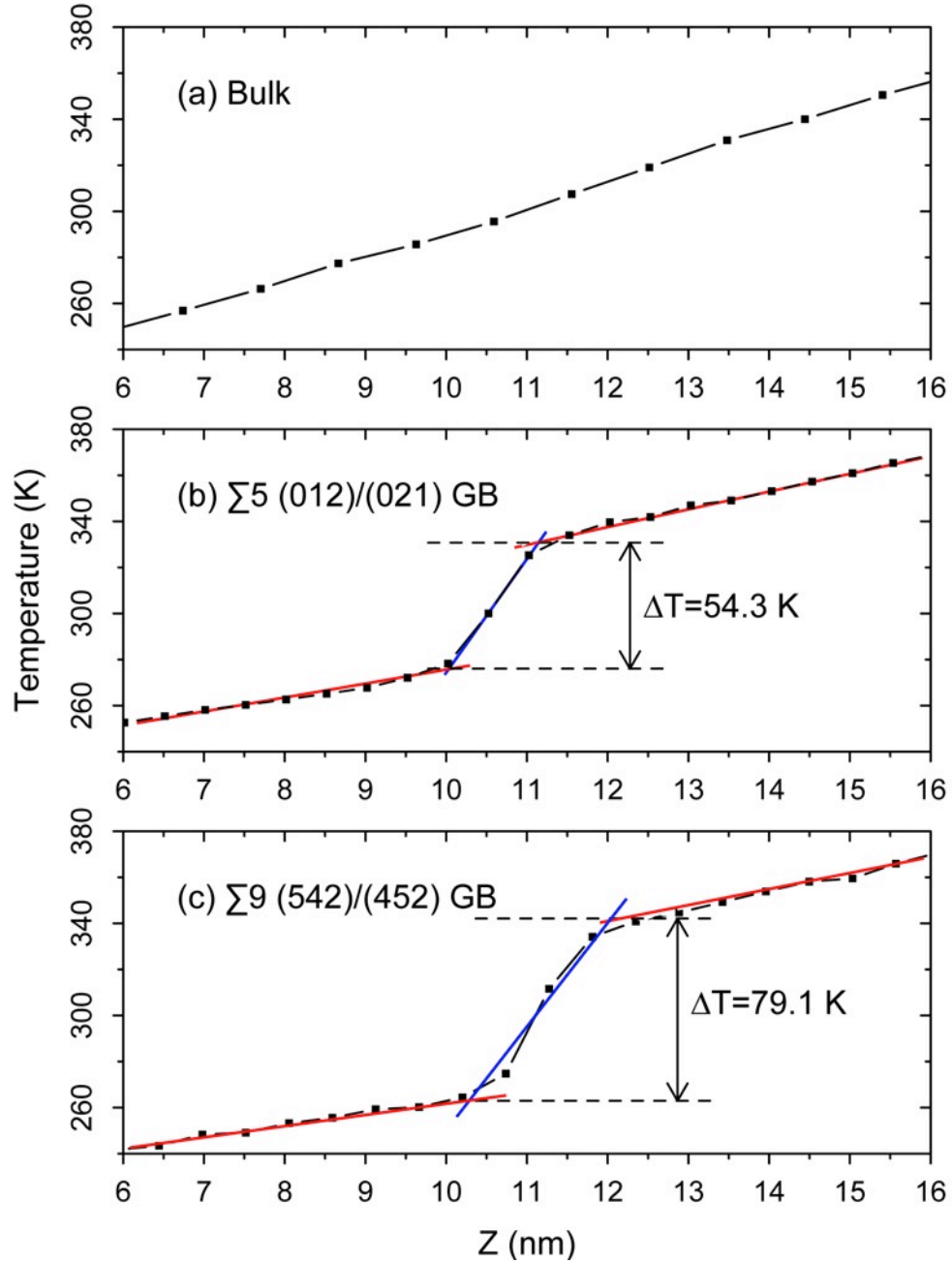


Figure 5.4: Temperature profile of UO_2 in bulk, $\Sigma 5$ (0 1 2)[1 0 0] and $\Sigma 9$ (5 4 2)/(4 5 2) bicrystal systems

5.2 The Kapitza resistance and grain boundary energy of CSL boundaries

We carried out calculations of the grain boundary energy γ , Kapitza resistance R and Kapitza length l_k for five different configurations, as summarized in Table 5.1. Although the data has certain fluctuations, there is a trend that R increases with increasing γ value. For example, for the $\Sigma 5$ (0 1 2)[1 1 0] boundary having $\gamma = 1.375$ J/m², R is about 0.512 Km²/GW. In a comparison, for the $\Sigma 9$ (5 4 2)/(4 5 2) boundary, γ increases to 1.788 J/m² and R increases to 0.781 Km²/GW. Besides, our result of the Kapitza resistance is in very good agreement with the preliminary results provided by Stanek, et al. [64]: our $\Sigma 5$ (0 3 1)[1 1 0] R value of 0.708 Km²/GW is very close to their calculated value of 0.73 Km²/GW. However our result of the Kapitza length is lower than theirs. The difference can be caused by our limited system size, which result in lower thermal conductivity values, and different interatomic potential. On the other hand, our Kapitza resistance is systematically lower than the values estimated by Watanabe et al. [33]. This is very possible due to the different system sizes, interatomic potentials, and grain shapes used [65]. As for our calculations of γ , we compare them to Van Brutzel's work [28] as shown in Fig. 5.5. Apparently, our GB energy values of the $\Sigma 13$ and $\Sigma 29$ cases are lower than Van Brutzel's, but the trend of values is still in agreement. These comparisons with other works prove validation of our calculation results.

Table 5.1: The Kapitza resistance, Kapitza length and energy of different CSL boundaries

CSL (Σ)	GB planes or GB plane and rotation axis	Dimension ($X \times Y \times Z$, in nm)	γ (J/m ²)	R (Km ² /GW)	l_k (nm)
5	(0 3 1)[1 0 0]	3.28×3.46×20.74	1.539±0.015	0.708±0.060	11.7±1.6
5	(0 1 2) [1 0 0]	3.83×3.67×20.55	1.375±0.010	0.512±0.034	7.7±0.8
9	(5 4 2)/(4 5 2)	3.28×3.67×22.01	1.788±0.012	0.781±0.047	14.1±1.3
13	(0 5 1) [1 0 0]	2.73×2.79×20.48	1.499±0.025	0.677±0.077	11.8±2.1
29	(0 5 2) [1 0 0]	2.73×2.95×20.41	1.637±0.017	0.681±0.070	11.2±1.9

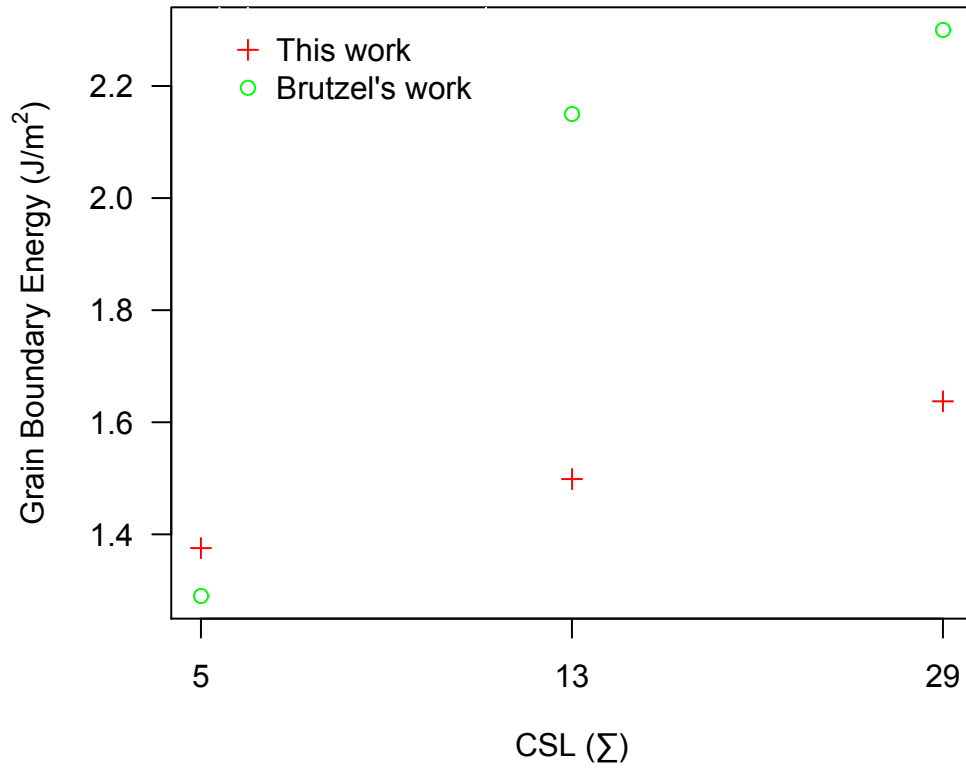


Figure 5.5: Comparison of the GB energy of our work with Van Brutzel's [28]

5.3 The effect of radiation damage on grain boundary properties

To reveal the effect of radiation damage on Kapitza resistances, three structures, $\Sigma 5$ (0 1 2)/[1 0 0], $\Sigma 9$ (5 4 2)/(4 5 2) and $\Sigma 13$ (0 5 1)[1 0 0], were selected for damage loading. They are picked because of their representations of low, intermediate and high R values as shown in Table 5.1, as well as their abundance in the CSL boundaries distribution suggested by experimental work [25]. From section 4, we learned that defects are loaded on to GBs by direct interaction. So we use three approaches of direct interaction between GBs and damage cascades to simulate the defect trapping in various irradiation conditions. One approach is to insert O/U interstitials on the surface of a GB and then use thermal annealing at ultra-high temperatures (2000-3000K) to speed up defect interaction with the GB. For $\Sigma 13$ system, this approach is used and two U atoms and four O atoms are loaded to the GB to remain electrical neutrality. The resulting relaxed defective structure is referred as $\Sigma 13R$. Another approach is to introduce a PKA of 2.3 keV near the boundary and then use high temperature annealing for defect removal and GB defect trapping. The number of defects loaded on the GB can be further adjusted by changing post-irradiation annealing temperatures. For $\Sigma 9$ system, this approach is used under constant volume and energy condition. After PKA creation, damage cascade annealing at 1000K, and final cooling down to 300K, a defective structure, referred as $\Sigma 9R$, is created. The third approach is to introduce multiple knock-on atoms to create successive damage cascades to maximize the defect trapping. For $\Sigma 5$ system, two 2.3 keV PKAs and post annealing at 1000K creates $\Sigma 5R$. If $\Sigma 5R$ is annealed additional at 2000K, then $\Sigma 5A1$ system is created. If the additional annealing

temperature is changed to 3000K, then $\Sigma 5A2$ system is created. In order to separate the effect of defects loaded on GBs from defects created in the bulk, the defect-loaded GBs, regardless of the methods for defect loading, are separated from the rest and re-inserted into a perfect lattice matrix. Therefore, there is no phonon-defect scattering within the bulk.

Figure 5.6 compares the boundary structures and mapping of energies of $[\phi(r_{ij}) - \phi_B]$ for atoms cross over GBs of $\Sigma 5$, $\Sigma 5R$ and $\Sigma 5A2$. X direction represents the top view of a GB, and corresponds to the rotating axis of the bicrystal to form the GB. Y direction represents the side view of a GB, and corresponds to the direction on the boundary plane but perpendicular to the rotating axis. Z direction is perpendicular to the boundary plane. Prior to ion irradiation, the atomic structure at the GB of $\Sigma 5$ is in form of CSL and shows pattern like configurations due to structural relaxation. After ion irradiation and boundary defect trapping, CSL is no longer perfect especially for oxygen atoms. This inevitably increases boundary energies. The projected energy mapping as a function of distance away from the boundary also suggests that the irradiated boundary has a wider distorted region. A careful comparison with disordered structures shows that the width change is caused by interface roughening, with the boundary defective band having zigzag features. Annealing, on the other hand, heals some of those broken CSL and brings atomic energy down.

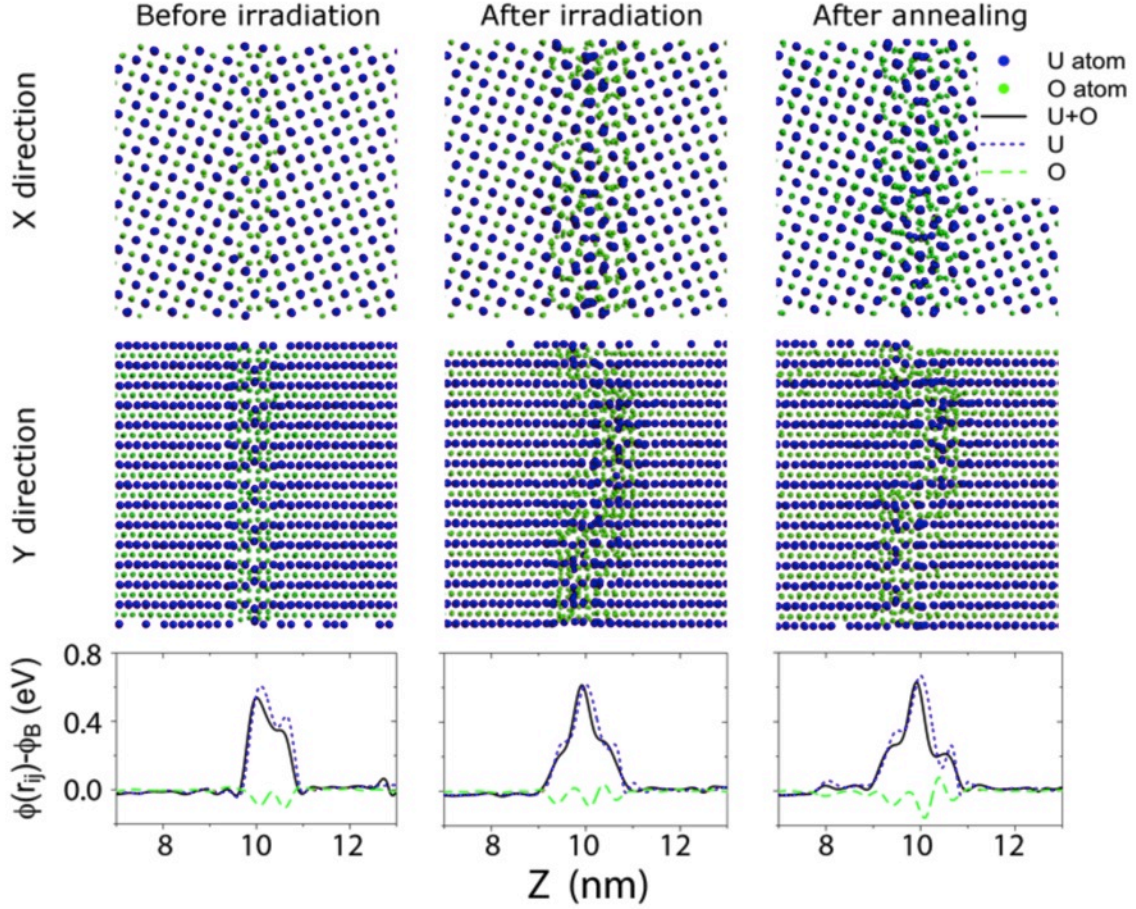


Figure 5.6: Atomic configurations and energies $[\phi(r_{ij}) - \phi_B]$ of UO_2 containing a $\Sigma 5$ (0 1 2)[1 0 0] grain boundary before introducing a damage cascade, after quenching of a damage cascade, and after post-damage-cascade annealing, respectively

Kapitza resistances of GBs with radiation damage are calculated with the same method as for unirradiated systems. The results are listed in Table 5.2. Compared to Table 5.1, it is obvious that defect-loaded GBs generally have enhanced values of γ , R and l_K . And the annealing at high temperature brings these values down, as the case of $\Sigma 5A2$. Furthermore, the Kapitza resistance shows a similar trend as the case of CSL boundaries: the higher the γ values, the higher the R values.

Table 5.2: The Kapitza resistance, Kapitza length and energy of defects loaded GBs

Structure	γ (J/m ²)	R (Km ² /GW)	l_k (nm)
Σ 13R	1.522±0.017	0.662±0.075	13.8±3.4
Σ 9R	1.884±0.016	0.956±0.080	18.1±2.6
Σ 5R	1.669±0.009	0.726±0.050	13.0±1.8
Σ 5A1	1.706±0.011	0.799±0.042	13.4±1.3
Σ 5A2	1.521±0.016	0.695±0.049	10.8±1.3

5.4 A correlation between the grain boundary Kapitza resistance and its energy

In order to develop a universal mode to describe the dependence of boundary thermal resistance on boundary energies, Fig. 5.7 combines the data from both unirradiated and irradiated cases. Each set of data shows certain fluctuations, but overall all data can be reasonably described by a simple formula:

$$R = A \times (e^{B\gamma} - 1)$$

where R is the Kapitza resistance of the GB, γ is GB energy. A and B are fitting parameters taking values of 0.34 Km²/GW and 1.55 m²/J, respectively. R decreases to zero as γ approaching zero. This is because $\gamma=0$ represents the case of a system without presence of a GB. And without the GB, ΔT must be zero and so as the Kapitza resistance.

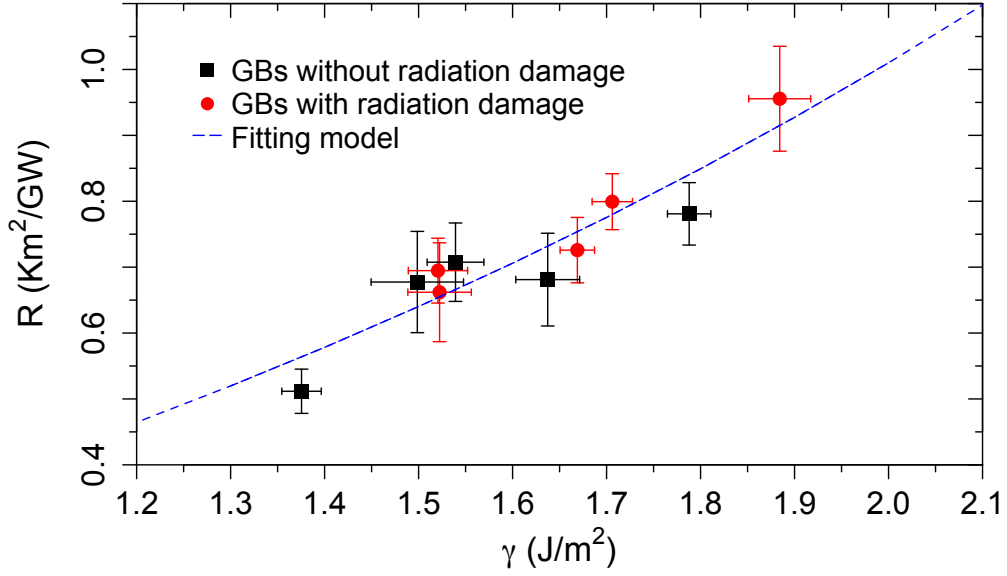


Figure 5.7: A plot of GB Kapitza resistances vs. GB energies for various configurations with or without radiation damage. The dash line refers to our fitting model

We fit the similar formula to the correlation of the Kapitza length l_k to GB energy as well, as shown in Fig. 5.8. The statistic error in l_k is more significant than it in R , due to the statistic error in thermal conductivities of the bulk. However the trend is still clear, and our A and B in this fitting take 3.48 nm and 0.94 m²/J respectively. Figure 5.9 shows the relationship between the Kapitza length and the Kapitza resistance. As expected, they are in a quite good linear relationship.

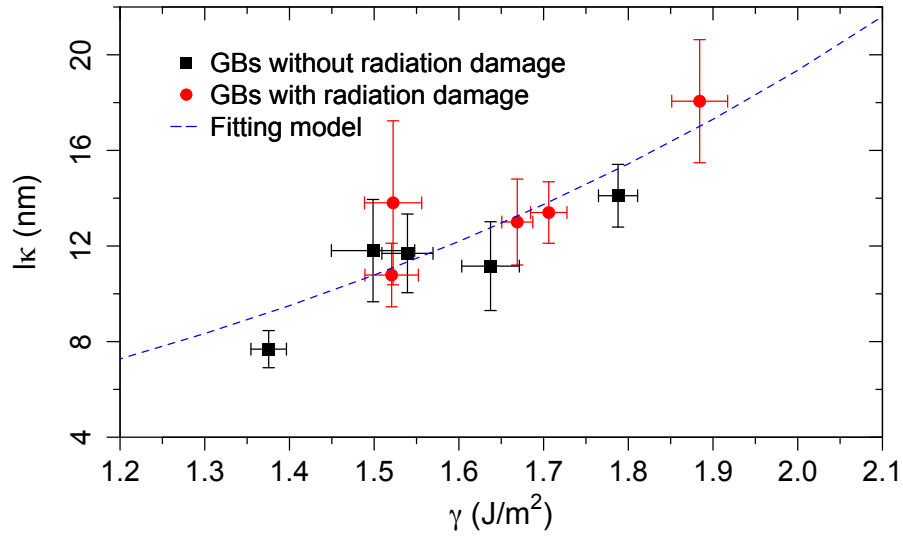


Figure 5.8: A plot of GB Kapitza lengths vs. GB energies for various configurations with or without radiation damage. The dash line refers to our fitting model

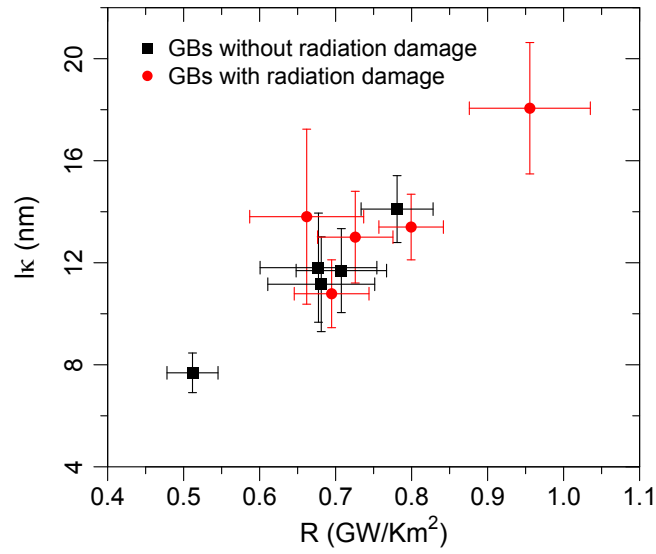


Figure 5.9: The correlation between the Kapitza length and the Kapitza resistance

6. SUMMARY

We studied both the evolution of GBs under different irradiation conditions and the Kapitza resistance of different GBs. We conducted a few comparable simulations for both parts of the study. In the formal part, we studied the interaction of GBs and defects like interstitials and vacancies in the uranium and oxygen matrix, the mechanisms by which GBs are loaded with defects and the structural change of GBs due to defect loading. In the latter part, we calculated the Kapitza resistance of different CSL boundaries, and investigated the change in Kapitza resistance due to damage cascade loading. Eventually, we revealed a general relation between GB energy and the corresponding Kapitza resistance.

We chose symmetric-tilt $\Sigma 5$ grain boundary to study the evolution of GBs under irradiation conditions. To introduce our damage cascades we assigned energy to a lattice atom to simulate damage by a PKA. To understand the interaction between GBs and damage cascades, we used two different energies for PKA. A high energy was used to simulate the case when ballistic-collision-mediated interaction between the damage cascade and GB. A lower energy was then used to simulate the case when the cascade creates defects in the close vicinity of the GB, which interact with the GB through interface biased defects migration. We also introduced the same damage cascades into monocrystal systems.

By analyzing the defects by comparing the simulated atoms final and initial positions, and examining the defect distributions as a function of time, we performed a couple of studies. First we compared the defect evolution in a GB system to those in a

mono-crystalline system, emphasizing the role the GB plays in absorbing defects. We also compared the difference in system mechanics when a damage cascade interacts with the GB. We found the same phenomenon reported in previous studies, that grain boundaries capture low-energy defects as they attempt to pass [27], and further found that it greatly enhanced the interaction between damage cascades and GBs, resulting in stronger defect trapping by the GB. We also found that GBs have a stronger trapping effect to oxygen interstitials compared to uranium interstitials, probably due to the lower migration energy of oxygen interstitials. Besides, the presence of uranium interstitials provides absorption to oxygen interstitials, and enhances the formation of interstitial clusters. Some of these clusters as well as point defects are tend to be trapped by the GB, and as a result, increase the energy of the GB.

Followed by the study of the evolution of GB under irradiation, we calculated the Kapitza resistance of different CSL GBs with and without defects loading. We started with 5 different CSL boundary systems roughly in the similar size to calculate their Kapitza resistance of the GB. The systems are firstly annealed at a high temperature for structural relaxation, before applying reverse non-equilibrium molecular dynamics to carry out Kapitza resistance calculations. Then we conducted radiation damages to selective CSL boundaries, to reveal the effect of defects loading to Kapitza resistance. To represent more situations, we employed three approaches to introduce radiation damage: inserting uranium and oxygen interstitials directly near GB, using a single PKA near GB to create defects, and using double PKAs with overlapping damage cascades. Before carrying out the calculation, defects in the bulk are carefully removed so that our

result reflects only the contribution from defect loading on the GBs. We found that a general correlation between GB energy and Kapitza resistance can be found, regardless of whether there is radiation damage or not. The higher energy GB has a higher Kapitza resistance. The energy of a GB is determined by its CSL type, its structure as well as its defects load. Usually, the energy of a GB increases after receiving radiation damage and trapping defects. And the annealing of the defect loaded GB at high temperature helps in structure relaxation and brings the GB energy as well as Kapitza resistance down.

REFERENCES

- [1] H. Stehle. (1988). Journal of Nuclear Materials, 153, 3-15.
- [2] IAEA. (2011). Impact of High Burnup Uranium Oxide and Mixed Uranium-Plutonium Oxide Water Reactor Fuel on Spent Fuel Management. Vienna.
- [3] M.C. Paraschiv, A. Paraschiv, V.V. Grecu. (2002). Journal of Nuclear Materials, 302, 109-124.
- [4] H. Assmann, W. Dörr, M. Peehs (1986). Journal of Nuclear Materials, 140, 1-6.
- [5] H. Assmann, H. Stehle. (1978). Nuclear Engineering and Design, 48, 49-67.
- [6] D. R. Olander. (1976). Fundamental Aspects of Nuclear Reactor Fuel Elements. Springfield, Virginia: US Department of Commerce.
- [7] J. Spino, J. Rest, W. Goll, C.T. Walker. (2005). Journal of Nuclear Materials, 346, 131-144.
- [8] A. Massih, K. Forsberg. (2008). Journal of Nuclear Materials, 377, 406-408.
- [9] S.F. Mughabghab, D.I. Garber. (1973). Neutron Cross Section, Vol. 1, Resonance Parameters. Upton, New York: US Report Brookhaven National Laboratory BNL 325.
- [10] H.J. Matzke. (1992). Journal of Nuclear Materials, 189, 141-148.
- [11] H.J. Matzke, H. Blank, M. Coquerelle, K. Lassmann, I.L.F. Ray, C.T. Woalker (1989). Journal of Nuclear Materials, 166, 165-178.
- [12] D. Brucklacher, W. Dienst (1972). Journal of Nuclear Materials, 42, 285-296.
- [13] M. T. Simnad. (2012). Nuclear Reactor Materials and Fuels. San Diego: University of California.

- [14] J. W. Harrison (1969). Journal of Nuclear Materials, 30, 319-323.
- [15] Y. Arai, T. Iwai, T. Ohmichi (1987). Journal of Nuclear Materials, 151, 63-71.
- [16] G.L.Hofman, L.C. Walters, T.H. Bauer (1997). Progress in Nuclear Energy, 31, 83-110.
- [17] C.M. Walter, G.H. Golden, N.J. Olson (1975). U-Pu-Zr Metal Alloy: a Potential Fuel for LMFBRS. Lemont, Illinois: Argonne National Laboratory.
- [18] G.L. Hofman, R.G.Pahl, C.E.Lahm, D.L.Porter (1990). Metallurgical Transactions A, 21A, 517-528.
- [19] K. Huang, Y. Park, A. Ewh, B.H. Sencer, J.R. Kennedy, K.R. Coffey, Y.H. Sohn (2012). Journal of Nuclear Materials, 424, 82-88.
- [20] R.C. Briant, A.M. Weinberg (1957). Nuclear Science and Engineering, 2, 797-803.
- [21] P. Browning (1980). Journal of Nuclear Materials, 92, 33-38.
- [22] R. Brandt, G. Haufler, G. Never (1976). Thermal Conductivity and Emittance of UO₂. West Lafayette, Indiana: Purdue Univeristy, Purdue Research Foundation, CINDAS.
- [23] C.G.S. Phillai, A.M. George (1993). Journal of Nuclear Materials, 200, 78-81.
- [24] L.A. Goldsmith, J.A.M. Douglas (1973). Journal of Nuclear Materials, 47, 31-42.
- [25] Nerikar, P., Rudman, K., Desai, T., Byler, D., Unal, C., McClellan, K., et al. (2011). Journal of American Ceramic Society, 94, 1893-1900.
- [26] G. Martin, P. Garcia, C. Sabathier, G. Carlot, T. Sauvage, P. Desgardin, C. Raepsaet, H. Khodja (2010). Nuclear Instruments and Methods in Physics Research B, 268, 2133-2137.

- [27] L. Van Brutzel, E. Vincent-Aublant, J. –M. Delaye (2009). Nuclear Instruments and Methods in Physics Research B, 267, 3013-3016.
- [28] L. Van Brutzel, E. Vincent-Aublant (2008). Journal of Nuclear Materials, 377, 522-527.
- [29] J. K. Mackenzie, (1958). Biometrika, 45, 229-240.
- [30] L. Lee, Research on the Molecular Structures and Nanostructures of Materials and Their Applications. Long Beach, California: The California State University:
<http://www.csupomona.edu/~lllee/wwwou/research.html>
- [31] K. Yamada, K. Kurosaki, M. Uno, S. Yamanaka (2000). Journal of Alloys and Compounds, 307, 10-16.
- [32] S. Nichenko, D. Staicu (2013). Journal of Nuclear Materials, 433, 297-304.
- [33] T. Watanabe, S. Sinnott, J. Tulenko, R. Grimes, P. Schelling, S. Phillpot (2008). Journal of Nuclear Materials, 375, 388-396.
- [34] D. C. Rapaport (2004). The Art of Molecular Dynamics Simulation. Cambridge: Cambridge University Press.
- [35] S. J. Plimpton (1995). Journal of Computational Physics, 117, 1-19.
- [36] S. M. Sze (1988). VLSI Technology. New York: McGraw-Hill.
- [37] L. Van Brutzel, J. Crocombette (2007). Nuclear Instruments and Methods in Physics Research B, 255, 141-145.
- [38] F. Müller-Plathe (1997). Journal of Chemical Physics, 106, 6082-6085.
- [39] A. McGaughey, M. Kaviani (2004). Physical Review B, 69, 094303-1-12.
- [40] J. Weber (1956). Physical Review, 101, 1620-1626.

- [41] D. Sellan, E. Landry, J. Turney, A. McGaughey, C. Amon (2010). *Physical Review B*, 81, 214305-1-10.
- [42] P. Schelling, S. Phillpot, P. Keblinski (2004). *Journal of Applied Physics*, 95, 6082-6091.
- [43] J. R. Walker, C.R.A. Catlow (1981). *Journal of Physics C*, 14, L979.
- [44] G. Busker (2002), Ph.D. thesis, Imperial College, London.
- [45] A. Ya. Kupryazhkin, A.N. Zhiganov, D.V. Risovany, K.A. Nekrasove, V.D. Risovany, V.N. Golovanov (2008). *Journal of Nuclear Materials*, 372, 233-238.
- [46] P. Goel, N. Choudhury, S.L. Chaplot (2008). *Journal of Nuclear Materials*, 377, 438-443.
- [47] N. –D. Morelon, D. Ghaleb, J. –M. Delhaye, L. Van Brutzel (2003). *Philosophical Magazine*, 83, 1533-1555.
- [48] K. Yamada, K. Kurosaki, M. Uno, S. Yamanaka (2000). *Journal of Alloys and Compounds*, 307, 1-9.
- [49] C.B. Basak, A.K. Sengupta, H.S. Kamath (2003). *Journal of Alloys and Compounds*, 360, 210-216.
- [50] T. Arima, S. Yamasaki, Y. Inagaki, K. Idemitsu (2005). *Journal of Alloys and Compounds*, 400, 43-50.
- [51] Si.I. Potashnikov, A.S. Boyarchenkov, K.A. Nekrasove, A. Ya. Kupryazhkin (2007). *ISJAEE* 8, 43-52.
- [52] E. Yakub, C. Ronchi, D. Staicu (2009). *Journal of Nuclear Materials*, 389, 119-126.
- [53] E. Yakub, C. Ronchi, D. Staicu (2010). *Journal of Nuclear Materials*, 400, 189-195.

- [54] B.G. Dick, A.W. Overhauser (1958). Physical Review, 112, 90-103.
- [55] K. Govers, S. Lemehow, M. Hou, M. Verwerft (2007). Journal of Nuclear Materials, 366, 161-177.
- [56] L. Pauling (1932). Journal of American Chemical Society, 54, 3570-3582.
- [57] S. Potashnikov, A. Boyarchenkov, K. Nekrasov, A. Kupryazhkin (2011). Journal of Nuclear Materials, 419, 217-225.
- [58] D. Manara, C. Ronchi, M. Sheindlin, M. Lewis, M. Brykin (2005). Journal of Nuclear Materials, 342, 148-163.
- [59] J. Ziegler, J. Biersack, U. Littmark (1985). The Stopping and Range of Ions in Matter. New York: Pergamon.
- [60] H. Ogawa (2003). GBstudio. staff.aist.go.jp/h.ogawa/GBstudio/
- [61] L. Van Brutzel, J. -M. Delaye, D. Ghaleb, M. Rarivomanantsoa (2003). Philosophical Magazine, 83 (36), 4083-4101.
- [62] S. P. Chen, A. F. Voter, D. J. Srolovitz (1987). Materials Research Society Symposia Proceedings, 81, 45-50.
- [63] P. Schelling, S. Phillpot, P. Keblinski (2002). Physics review B, 65 (14), 144306-144318.
- [64] C. Stanek, et.al (2010). Lower Length Scale Simulations of Transport in Oxide Fuels. New Mexico: Los Alamos National Labrotary.
- [65] X. Wang, Y. Yang, L. Zhu (2011). Journal of Applied Physics, 110 (2), 024312-1-6.